A surface science investigation of ZnS (001) single crystal

By:

Pablo Ribeiro Alves de Oliveira

Advisor:
Dr. Fernando Loureiro Stavale Junior

A thesis submitted in partial fullfilment of
the requirements for the degree of

Master of Physics

at the

CENTRO BRASILEIRO DE PESQUISAS FÍSICAS

August 2021

“A SURFACE SCIENCE INVESTIGATION OF ZnS (001) SINGLE CRYSTAL”

PABLO RIBEIRO ALVES DE OLIVEIRA

Dissertação de Mestrado em Física, apresentada no Centro Brasileiro de Pesquisas Físicas do Ministério da Ciência, Tecnologia, Inovações e Comunicações. Fazendo parte da banca examinadora os seguintes professores:

Fernando Loureiro Stavale Junior – Presidente/Orientador/CBPF

Abner de Siervo- UNICAMP

Luiz Carlos Sampaio Lima - CBPF

Rio de Janeiro, 06 de agosto de 2021.

"*Hard work beats talent*"

Acknowledgements

I would like firstly to thank God for all. In the sequence, I would like to thank each person that has contributed to my work and career either directly or indirectly. In this regard, I must emphasize some names:

My advisor, Fernando Stavale, for all patience and teaching, especially for being a group leader instead to a simple boss.

Professor Pedro Venezuela, from UFF, for all patience and for introducing me to DFT, then facilitating the combination of both experimental results and theoretical calculations, which is one of the main wishes to the sequence of my career.

All my Surface and Interface Phenomena Group (SIPG) colleagues, especially Rubem, Astrid, Bianca, and Guilherme, for all assistance in the experiments and the fun times that relieve everyday stress. I must highlight Guilherme, for all scientific discussion and for his brilliant mastery of scientific instrumentation, which makes him the SIPG "philosopher's stone".

All colleagues from Pedros group, especially Rodolfo, for the fruitful discussions and meetings full of high-level Physics. I must also thank my old graduate friend Emmanuel for his support in times of distress, especially before the PhD interview, and also to the excellent virtual meetings with exciting discussions about Physics.

All CBPF members, from teachers to guards (especially André, who despite being Flamenguista is a good people) for dealing well with such an adverse situation as the one we are experiencing due to the Covid 19 pandemic.

My parents, Honorino and Sueli, my brothers, Patrick (and his dog Hunter) and Patrício (as well as dear "Mota" and "Motinha" and my "big friend" Filipe), my sister Luiza (and my niece Rebeca), my uncle Zeca, and my friends Paulo and Jhonny (as well as their family), for all the support, cheering and affection through my entire life that despite the 1110 km distance during the last two years were essential to get here.

My bride's family, especially her parents ("Seu Anselmo" and Daniela), for the affection and trust. And to my bride Fernanda, for all patience, companionship, and love, which overcome any distance.

Finally, I thank CNPQ for funding this research, as well as CENAPAD for the computational support. Furthermore, I thank all other national agencies (CAPES and FAPE (RJ, SP, MG, etc.) for believing in science.

Contents

List of Figures

List of Tables

Resumo

Esta dissertação apresenta um estudo de ciência de superfície das propriedades do monocristal ZnS (001) utilizando espectroscopia de fotoelétrons excitados por raio-X (XPS) e difração de elétrons de baixa energia (LEED). Para alguns achados experimentais, que são a parte fundamental desta investigação, buscamos um suporte teórico utilizando cálculos de primeiros princípios baseados na Teorida do Funcional da Densidade (DFT). Nós objetivamos converter o compartamento isolante da superfície deste material numa estrutura semicondutora. Para tanto, a preparação da amostra por ciclos combinados de desbaste iônico e tratamento térmico foi empregada. Os achados experimentais revelam que tal metodologia dá origem a uma estrutura mais rica em enxofre. Então especulamos que os ciclos de tratamento de superfície favorecem a remoção de átomos de Zinco. Baseado nesses resultados, é proposto um modelo empírico consistindo de uma reconstrução de superfície do tipo (1 x 2) caracterizada por linhas alternadas de átomos de Zinco faltantes. Em vista da correção na posição da energia de ligação no XPS e o padrão de difração obtido com o LEED, pode-se especular que este cenário (superfície reconstruída e mais rica em Enxofre) pode melhorar a condutividade na superfície do ZnS. Uma assinatura indireta de tal hipótese foi obtida através de cáculos de estrutura de banda que revelaram vários estados de superfície com um aspecto semi-metálico preenchendo a zona proibída.

Abstract

This work present a surface science investigation on the properties of the ZnS (001) single-crystal by X-ray Photoelectron Spectroscopy (XPS) and Low Energy Electron Diffraction (LEED). Besides the experimental results, which are the heart of this thesis, we performed some first-principles calculations based on the Density Functional Theory (DFT) in view to rationalize some speculations derived by the experiments. We aim to convert the insulating behavior of the ZnS surface into a semiconducting structure. In this regard, we perform several cycles of sputtering followed by thermal annealing. The experimental findings reveal that this methodology leads the formation of a s-richer structure. Then we speculated that the surface treatment favors the removal of zinc atoms. Based on this finding, we purposed a empirical model consisting of a (1 x 2) surface reconstruction characterized by alternating missing row of Zn atoms. In view of the correction on the binding energies positions in XPS experiments and the LEED patterns, one can speculate that this scenario (reconstructed and s-richer surface) might increase the surface conductivity of the ZnS system. An indirect assignment of such an hypothesis was derived by band structure calculations, which revealed several surface states with a semi-metallic like character filling the forbidden zone.

Chapter 1

Introduction

1.1 General aspects

Semiconductor physics is perhaps one of the most important areas of modern science and technology. Several breakthroughs in this field such as thermionic emission theory, light emission diode (LED), and transistors, to mention a few, led to exciting achievements in 21^{st} century, such as integrated circuits and high-performance nano-devices. [1, 2]. Despite this large interest in applications, semiconductor physics is, in addition, one of the most investigated fields with thousands of papers published related to this theme [1]. The discovery of novel materials and possibilities to achieve even better conditions of application with them, are the main reported topics among these publications. Besides these novel materials, sulfide structures made up by a transition metal bond to Sulfur species are of particular interest, being zinc sulfide (ZnS) one of the main investigated structures [3].

ZnS is a binary semiconductor that belongs to the II-VI class [4]. It can be found with two different phases: zinc blende (ZB), with a lattice parameter of 5.41 Å and a direct band gap of 3.7 eV [5], and wurtzite (WZ) with 3.82 Å and 3.7 eV for the lattice parameter and the energy gap, respectively [6]. Notability, zinc blende structure is the most stable at room temperature, while WZ-ZnS tends to be dominant at elevated temperatures and pressures . Both structures are illustrated bellow in Figure 1.1 There are some particularities that turn ZnS into a recipient for a wide range of applications. Among these we can mention the elevated melting point, high index refraction, and the aforementioned direct wide- band gap, crucial factors for infrared optics and solar cells applications, for instance [7].

These different fields of interest are reflected in the growing increase of re-

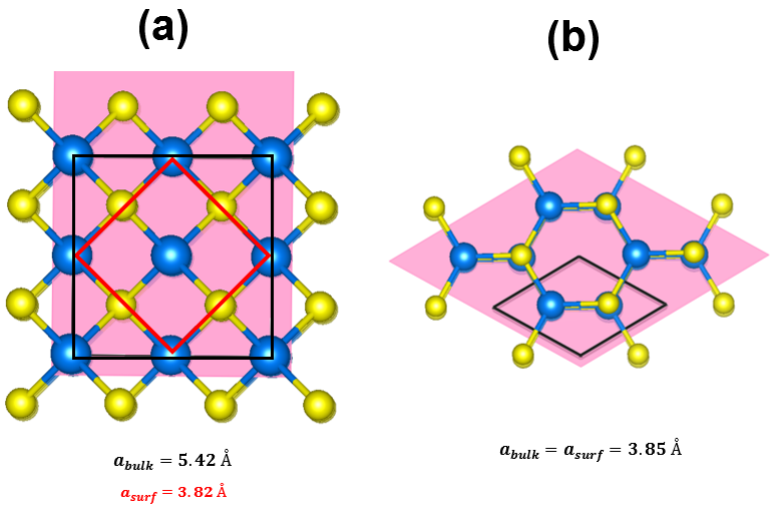

Figure 1.1: ZnS main phases. *Zinc (light-blue balls) bonding to sulfur (yellow balls) at (a) zinc blende in (100) plane and (b) wurtzite arrangement in (0001) plane. [8].*

searches that involve ZnS, as illustrated in Figure 1.2. It is worth noting the especial increase of interest on ZnS in the nano-era that has been started from innovation experiments with graphene, carried out by *Novosolev and Geim* [9]. During this period, different ZnS nano-structures have been received special attention, such as ZnS hollow sphere, 3D ZnS architectures assembled by 1D structures, ZnS nanowire, ZnS nanobelts, and ZnS thin films [10–13]. Each nanostructure has its own peculiarities that can be addressed to different factors. A comprehensive understanding of the major role that drives their unique electronic and geometrical properties might be crucial for a complete advance in this field.

However, this dissertation does not attempt to evaluate all the particularities of each nanostructure. Instead, it aims to investigate the electronic and crystallographic properties of the ZnS surface in the most stable configuration (cubic phase). An unequivocally unveiling of the fundamental parameters in such properties can be very useful to realize the crucial factor(s) of some unusual properties in the ZnS surface. In this context, researches carried out with a high purity sample and avoiding external contaminants are of great interest. Hence, ZnS single-crystals and ultra high vacuum (UHV) conditions are essentials. UHV conditions are mandatory especially when surface-sensitive techniques like X-ray photoelectron spectroscopy (XPS) and low energy electron diffraction (LEED) are carried out [1].

These aforementioned techniques are powerful tools for a complete understanding of the chemical status of the sample and its crystallographic structure, respectively [14]. Nevertheless in poor conductivity systems XPS, and especially LEED

[1] See chapter 3 for an extended discussion on these topics

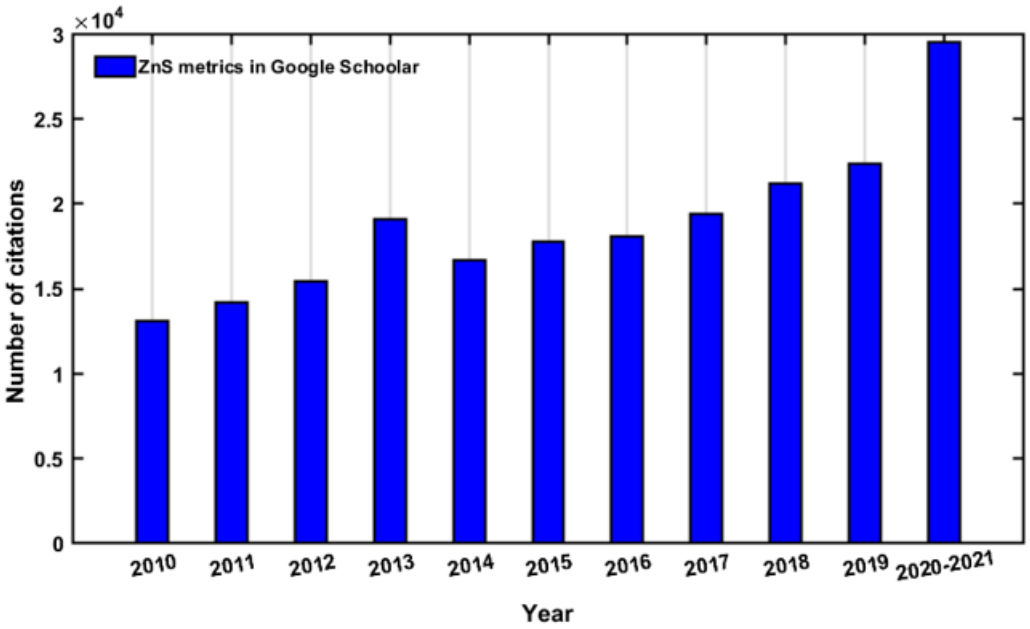

Figure 1.2: ZnS Metrics*. Data acquired from Google Scholar using "Zinc Sulfide" as keyword .*

investigations, are strongly tampered [15]. Since ZnS has an elevated resistivity (of the order of Peta ohms), one of the main challenges in this investigation is to convert the insulating behavior of ZnS surface into a semiconducting one.

In view of this, different scenarios of surface treatment will be carefully examined. Such a treatment consisting of combined cycles of ion sputtering and thermal annealing, and it is well established in the literature as the main route for in-situ surface preparation. Preparation conditions, especially the annealing temperature, can drive dramatic changes in the sample. In this work, we reported that the higher annealing temperature, the higher the S/Zn ratio, thus indicating a prevalence of sulfur over zinc species at the outermost layers of the ZnS surface. In addition, we speculated that this scenario favors a surface reconstruction along [110] direction consisting of alternated row of missing zinc atoms, corresponding to a (1 x 2) unit cell. In this scenario, we expect a more semiconducting behavior of the ZnS surface, translated into new states lying in the forbidden zone and tailing the gap. Such hypotheses will be investigated by combining experimental and theoretical tools.

1.2 Outline

In this work, we investigate the structure of ZnS (001) single crystal surface by XPS and LEED, together with some first-principles calculations based on the density functional theory (DFT). To achieve this, the dissertation is organized as follow:

- Chapter 2: A brief discussion on chemical bonds, electronic structure and thermodynamical aspects of semiconductors with particular interest on the their surface properties . The major role that drives surface transformation will be emphasized.

- Chapter 3: The experimental methodology will be discussed in details. XPS and LEED technique will be explained from qualitative to quantitative point of view, in order to connect the main physical concepts with the experimental findings. The sample preparation in both scenario, vacuum conditions and DFT framework (upon slab method preparation) will be also highlighted.

- Chapter 4: The main results of this research will be discussed and divided into two sections. First, we show the insulating behavior of the sample, and how this property has influence on XPS and LEED experiments. Following that, we evaluate the degree of influence of intensive surface preparation conditions (high annealing temperature) on the ZnS surface by XPS and LEED experiments. We close the chapter by examining a particular speculation derived from the experiments through DFT calculations.

- Chapter 5: We summarize the main ideas reported in this thesis and discuss some of the thoughts and perspectives for the next steps towards a complete understanding of sulfide structures.

We close this research with two appendices exploring the fundamental aspects of DFT calculations and the effects of cation vacancy on the ZnS system, respectively.

Chapter 2

Basic Concepts and background

In this chapter, we discuss qualitatively some important topics related to the properties of semiconductors, such as chemical bonds and band gap. Regarding to semiconductors surface, we will emphasize both aspects polarity and stability. The role of surface preparation, with special attention on the influence of pressure and temperature will be discussed from a thermodynamical point of view.

2.1 Chemical bond and electrical behavior

It is well known that the way how atoms bond themselves plays a crucial role in the crystallographic arrangement. Therefore, an important starting point of discussion is ionicity. Such a parameter will measures what type of bond is more significant in the structure and could be described as [16]:

$$f_i + f_c = 1. \tag{2.1}$$

Here, f_i and f_c take into account the contributions of ionic and covalent bonds, respectively. According to the model purposed by *Philips*, f_i can be defined in terms of the energy splitting E_h between bonding and anti bonding levels, together with a constant C proportional to the difference of electronegativities between the atoms in the particular structure under consideration [17]:

$$f_i = \frac{C^2}{E_h^2 + C^2} \tag{2.2}$$

The mentioned bond differs from the major interaction which intermediates the process. Ionic bonds are characterized by a transference of valence electrons from an atom to another. Hence, there is an electrostatic attraction between the cation and the anion. On the other hand, if the valence electrons remain

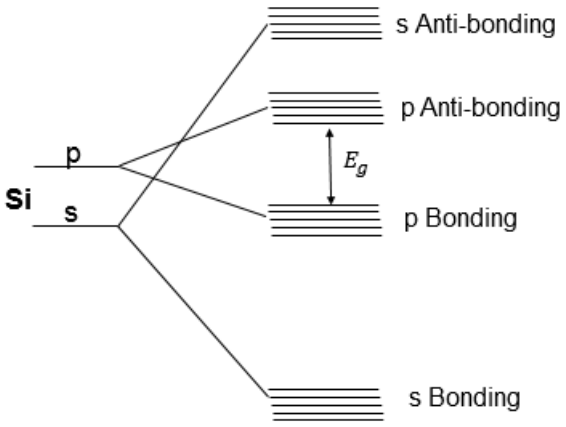

Figure 2.1: Energy level diagram of silicon. *Adapted from[19]*

localized between two atoms, the so-called exchange interactions - resulted from the overlapping of atomic orbitals - arise, and hence covalent bonds are formed [18].

For instance,the overlapping of $3s$ and $3p$ orbitals in silicon (Si) gives rise to bonding and anti-bonding states. Each state will be broadened into a band by increasing the number of silicon atoms. Such bands will be composed of filled and unfilled states. The unfilled s and p states will lie in the region called conduction band, and the filled p and s states in the valence band. These regions will be separated by a gap, called energy gap [1],which corresponds to the minimum energy required to promote an electron from a filled to an unfilled state. An illustration of Si electronic structure in a energy level diagram representation is shown in Figure 2.1.

The band gap is a criterion that allows to grade the materials as conductor, semiconductor, and insulator. Of particular interest, semiconductors compounds can in addition be ranked into three main categories according to their gap: (i) *conventional*, whose band gap falls in the range of 1-2 eV ; (ii) *wide-band gap* (WBG), related to material with E_g of order of 3-4 eV ; and (iii) *ultra-wide band gap* (UWBG), for structures with E_g higher than 4 eV [3]. Typically, binary semiconductors consisting of a transition metal plus a chalcogenide/oxide belongs to the WG class. Some of such compounds and their band gap are grepped in table 2.1.

[1]This quantity emerges naturally due to the periodic potential in the lattice. See Kroning-Penny model, for instance [17]

Class	Structure	band gap (eV)
Oxides	ZnO	3.4
	MnO	3.3
	CuO	2.8
Chalcogenide	MnS	3.4
	ZnS	3.6
	ZnSe	3.2

Table 2.1: Band gap of some binary wide-band gap semiconductors. *Adapted from [16]*

Returning to the issue of crystal arrangements and chemical bonds, it is worth taking a bit of comment on a common and interesting structure called zinc blende. By replacing the centers and the corner of tetrahedral in the diamond structure for atoms from the groups III and V, respectively, the ZB structure is formed [20]. In this construction there is some migration of the negative charge from species V to III, hence there are partially covalent and partially ionic bond contributions.

In the same vein, $II - VI$ group can give rise to a zinc blende structure. However, there is no equal contribution of ionic and covalent bond, being the last the dominant one. This prevalence of covalent bond implies a larger ionicity in comparison with the III-V group, as shown in table 2.2.

System	Material	Ionicity
III-V	GaP	0.32
	GaAs	0.31
	InP	0.42
II-VI	ZnO	0.61
	ZnS	0.62
	ZnSe	0.63

Table 2.2: Philips ionicity for some III-V and II-VI binary semiconductors.[16]

Typically, the higher the ionicity is, the higher is the band gap. This fact tends to implies an insulating behavior of covalent structures, such as diamond and carbon disulfide. One remarkable property of insulating systems is the low number of majority carriers. Such carriers are electrons in the conduction band and holes at the valence band. One can decrease the amount of energy required to promote electrons (holes) to the conduction (valence) band, by populating the forbidden zone. This scenario can be achieved by the doping process, either by adding a foreign atom into the lattice or by removing a natural specimen of the structure, for instance. Both aspects will be considered next.

2.2 Brief comments on defects in semiconductors

There are two main groups of defects in semiconductor physics: The intrinsic, which involves only atoms from its own structure, and the extrinsic, which is composed by external impurities [21]. Intrinsic defects are also known as "native" defects (herein we will adopt such a nomenclature) and can be divided into four different classes [21]:

- *Vacancy*, which is created by a missing atom A (V_A);
- *Interstitial*, obtained when an atom A occupying an interstitial site in the host crystal (I_A);
- *Schottky defect*, corresponding to a host atom that leaves it position and moves to the surface, then forming a vacancy ;
- *Frenkel-Defect*, corresponding to a host atom that moves to an interstitial position, giving rise to a vacancy-intersite pair.

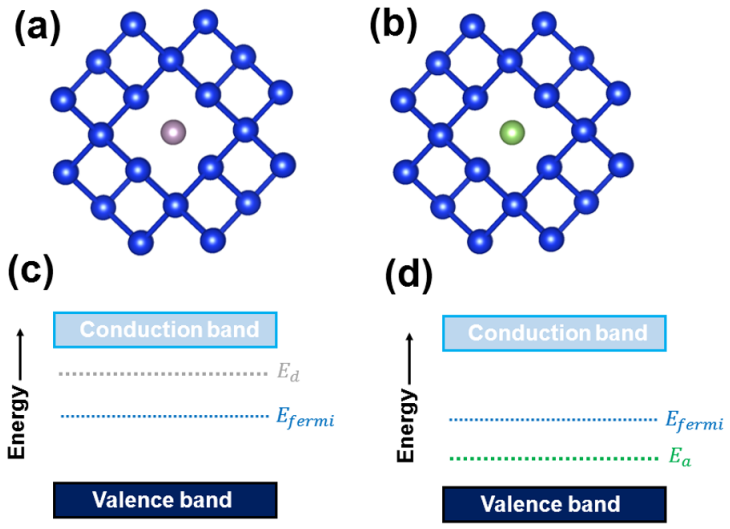

Figure 2.2: n and p-type doping in the Si lattice. *Si structure (blue balls) doped with (a) Phosphorus (gray ball) ; (b) Gallium (green ball) ; Energy level diagram for (c) donor doping , (d) acceptor doping. Adapted from [19].*

Intrinsic and extrinsic defects can yield extra electronic levels in the forbidden zone. If such levels lie nearby the conduction or valence band, they are called *shallow levels*. On the contrary, if these levels are found in the middle of the gap, they configure *deep levels*. For convenience, we will focus the discussion on the first category. The electronic position of these levels depends on the nature of "extra" contributions. Consider firstly the extrinsic impurities. If the contributions arise

from free electrons, then the shallow levels are addressed to *donor* levels and the doping is often classified as n-type doping with such levels lying slightly below the conduction band [19]. This scenario is illustrated in Figure 2.2-(a) by the replacement of a silicon atom by an atom from group V, which has one more valence electron. This extra valence electron is weakly bond with Si atoms. Then it can be easily excited from the donors level E_d to the conduction band without creating holes in the valence band, as illustrated in Figure 2.2-(c).

Conversely, defects that contribute with holes give rise to shallow levels slightly above the valence band and are related to *acceptor* levels [19]. Such a configuration can be obtained by replacing the Si atom with an atom from group-III - as depicted in Figure 2.2-(b) - which has one less valence electron. Typically, this extra level reaches its energy minimum with one more bond. Then Si atoms are expected to compensate the difference of charge through a new bond with this defect, leading the migration of electrons from valence band to this new energy level called acceptor level (E_a), as depicted in 2.2 -(d).

Among intrinsic defects, of particular interest in this investigation are vacancies. This kind of defect can also induce states in the forbidden zone. The nature of such states depends on the chemical status of the absent specimen. Generally, anion vacancy behaves like donors and then induces states above the Fermi level. On the other hand, cation vacancy behaves similarly to acceptors. Hence its state will lie slightly above the valence band. Such states are addressed to dangling bonds, which are related to a decrease in the coordination number [19].

In the case of surfaces, their own formation leads states on the gap [22]. This fact results from broken bonds that are a natural process when a surface is obtained. Even in the ideal case - the absence of electronic redistribution- there will remain unbonded hybrids, which originate such surface states [22]. Consider the zinc blende structure. Whereas the bulk atoms are four-fold, the species at the outermost layers are three-fold. Thus, there will be at least one broken bond at its outermost layers. In the particular case of ZnS, the removal of a zinc atom increases the number of broken bonds by leaving two more sulfur dangling hybrids. This process is illustrated in figure 2.3

The removal of some specimens at the surface could be an interesting strategy in order to achieve one of the two major requirements of a surface: a minimum of polarity. Therefore, a surface rearrangement must be preferential if surface dipoles are present, and then, geometrical modifications at the surfaces are expected. In terms of surface polarity, an especial discussion arises from the *Tasker's surface* model [23]. This issue along with some important aspects of surface structure will be emphasized next.

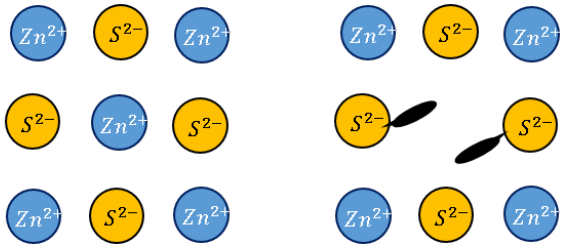

Figure 2.3: Dangling bonds in the ZnS Structure.

2.3 Surface polarity

The role of polarity on surface arrangements has been widely discussed for several systems, especially for metal oxide surfaces, as presented by [24]. Foundations of this issue have been derived by *Tasker*, which purposed three possible architectures for ionic and partly ionic surfaces classified in terms of dipoles moment contributions to the surface [25]. It is worth keeping in mind that surfaces can be investigated by assuming the crystal as a stacking of planes. In this context, and according to the Tasker's theory, there are three fundamental categories of surfaces called Type I, II, and III. These structures are illustrated in 2.4 (a)-(c).

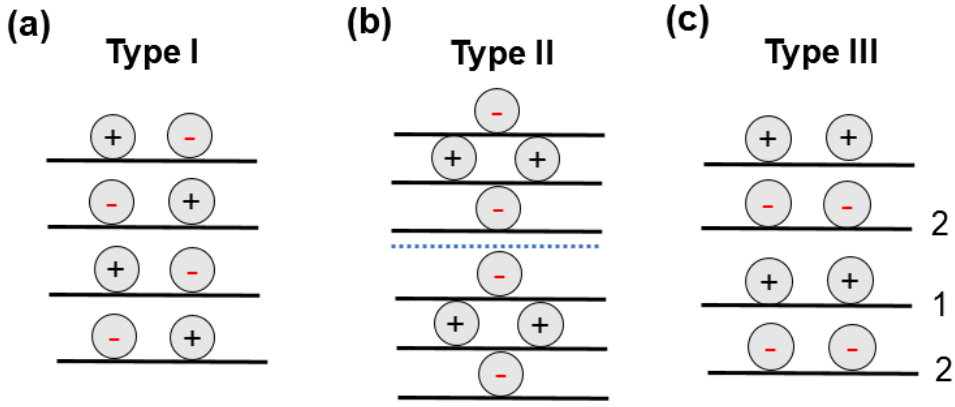

Figure 2.4: Tasker Surface *(a) Type I, (b) Type II , and (c) Type 3. Adapted from [25]*

Type I surface is non-polar since it consists of anion and cations in a stoichiometric ratio. Although Type II surface consisting of a stacking of charged planes, there is no dipole moment perpendicular to the surface. This arises from the symmetrical configuration of such an arrangement, with each plane equally contributing to the electric field, but with opposite signal, resulting in a zero dipole moment. On the other hand, Type III surface is a polar structure. This can be explained if we consider an ion on plane 1 of Figure 2.4. The field from the surrounding planes, labeled as 2, is cancelled out by symmetry. However, at the outermost layer, we are left with the field which is not canceled by any neutral

crystal block [25].

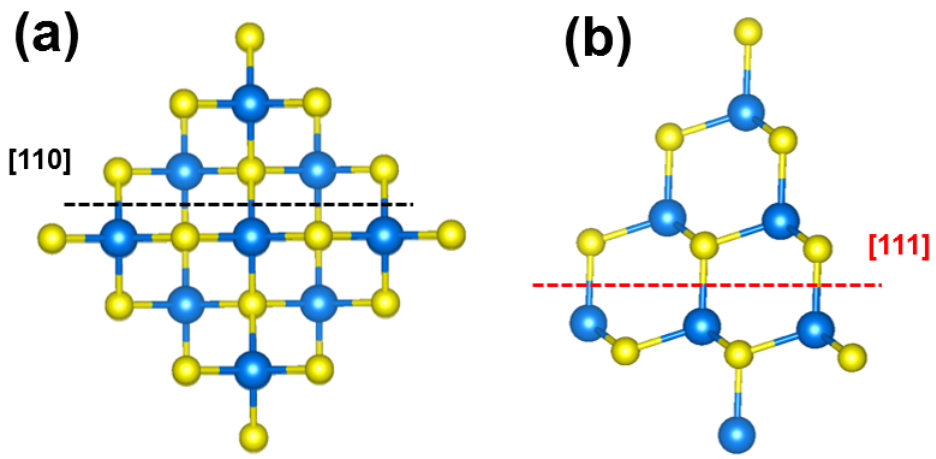

Figure 2.5: Different cleavage directions in ZB structure. *(a) cleaving along [110] direction ; (b) cleaving along [111] direction. Authorial illustration.*

As mentioned at the end of the preceding section, a surface must to minimize its polarity. Then, based on this aspect, one can explain the stability of the zinc blende structure, which is a crucial aspect to understand the preferential cleaving direction, for instance. Consider Figure 2.5. Along the [111] direction - Figure 2.5-(b) - there are different terminations among the upper and lower layers, which is favorable to the electrostatic attraction among them. Hence, it will require a larger amount of energy to separate these layers. Conversely, from Figure 2.5-(a), one can note that by separating the layers along [110] direction the system is left with equivalents termination, then no overall of electrostatic force will take place, which turns this plane the most energetically favorable to be cleaved, as attested by *Ebert et al.* [26].

In view of the present discussion, it seem evident that polar surfaces tend to be unstable. For this reason, such structures can only occur by removing the dipole contributions perpendicular to the surface. This can be achieved by geometrical reconstruction, originated by point defects, for instance. Such a process can be explained as follow. By removing an atom, the number of dangling hybrids will increase as far. The natural tendency is fresh recombination among the remaining atoms towards a new ground state (which in the case of surfaces means a minimum of surface-free energy, as will be discussed soon). In this process, deviations in the atomic position might occur in such a way that the length of a sequential chain is not the same in all directions, which results in a translation symmetry breaking. This process is well-known as geometrical *reconstruction*. Besides point defects, temperature can also drives to dramatic surface modifications. The role of some

thermodynamics quantities such as temperature and pressure will be emphasized next.

2.4 Thermodynamics considerations on surface stability

An elegant discussion about surface stability is made from thermodynamic point of view. In this scenario, the equilibrium properties of matter will be derived as function of macroscopic parameters.

Initially, consider the Gibbs picture of the *dividing surface* [22]. In this context, two homogeneous regions of volumes V_1 and V_2, respectively, are separated by a boundary surface corresponding to a plane at an arbitrary position z_s, as depicted in Figure 2.6

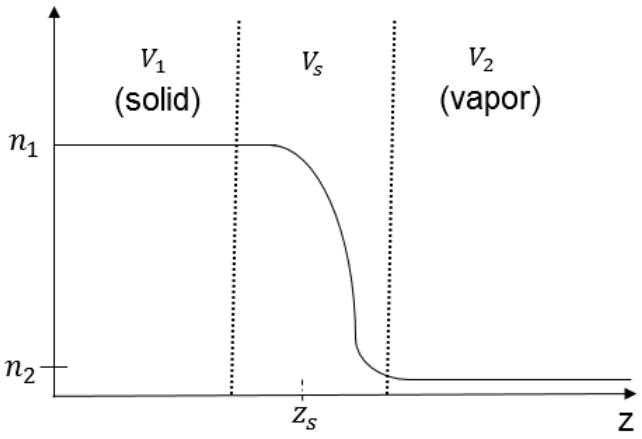

***Figure 2.6: Gibbs Scenarios**. Adapted from [22].*

For the sake of simplicity, let us consider as the extensive variable describing the system the total number of particles, N_i, and choose z_s in such a way that the number of particles at the surface are negligible, i.e, $n_s = 0$. With such an assumption, we can write [27]:

$$N_i = n_1 V_1 + n_2 V_2. \tag{2.3}$$

Once the dividing surface is defined, we can express the surface thermodynamical quantities. For this, it is worth to remember that system transformations occurring at a constant temperature (T), volume (V) , and chemical potential (μ_i) are conveniently described in terms of the *grand potential* [2] Ω. Similarly to Gibbs free energy G, it is an extensive function of only a single extensive variable (V).

[2] In some references called *Kramer's grand potential[22]*

Since Gibbs free energy has as extensive variable the number of particles N and one can express it as

$$G = \mu N, \tag{2.4}$$

then it is expected that the gran potential be proportional to V. Since

$$\left(\frac{\partial \Omega}{\partial V}\right)_{\mu,T} = -p, \tag{2.5}$$

thus

$$\Omega = -pV, \tag{2.6}$$

which is equivalent to the definition showed by *Bechstedt* in terms of the Helmholtz F and Gibbs G free energy [22]:

$$\Omega = F - G. \tag{2.7}$$

In the dividing surface picture, the Kramer's Grand Potential can be written as function of the contributions from phases 1 and 2 plus a surface term, i.e:

$$\Omega = -p(V_1 + V_2) + \Omega_s. \tag{2.8}$$

The surface contribution Ω_s should be proportional to the surface area A

$$\Omega_s = \gamma A. \tag{2.9}$$

On the Gibbs assumption with $N_S = n_s A = 0$, the surface contribution for the free enthalpy is neglected. Therefore,

$$F_s = \Omega_s = \gamma A, \tag{2.10}$$

or in terms of the free entropy S_s, and surface Internal Energy U_s

$$\gamma = \frac{U_s - TS_s}{A}. \tag{2.11}$$

The surface free energy (γ) is isotropic in the case of liquids, however, there is function a crystallographic orientation dependence in the case of crystalline solids. Effects like lattice vibrations and surface polarity tend to influence the surface free energy. The first is addressed to thermal fluctuations, related to the mean square deviations of the atomic position with respect to the average position [27]. Each plane possesses its own vibration mode, and therefore different contributions to the surface entropy can arise, as discussed by *Desjonquères and Spanjaard* [27].

The latter point implies a buckling effect, that changes the equilibrium shape of crystal (ECS) derived from Wuff theorem [22]. When anisotropic crystals are regarded, the surface free energy will be minimized from a particular direction apart out from the normal plane, then resulting in the formation of facets [22]. This crystallographic dependence can in addition be qualitatively understood in terms of broken bonds. By minimizing the number of dangling hybrids, a minimum of surface free energy will result. Considering the diamond structure, it is clear from Figure 2.7 that cleaving the structure along [111] direction requires a lower number of nearest-neighbor atoms to be removed in order to create a surface in comparison with the cleaving along [100] direction.

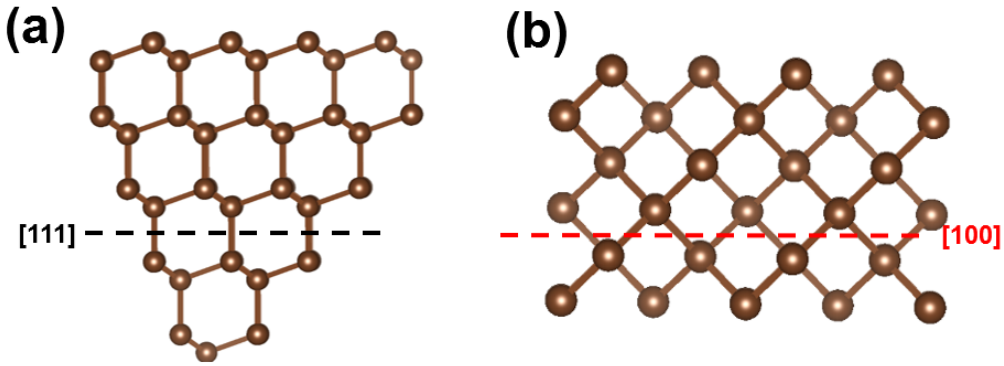

Figure 2.7: Cleavage directions in the Diamond structure. *(a) Cleaving along [111] direction. (b) cleaving along [100] direction. Authorial illustration.*

Therefore it is expected that surface with this orientation requires less amount of energy to be obtained, and hence be the preferential one to be cleaved, for instance. This expectation is widely confirmed [16].

Thus considering such arguments, it is convenient emphasize the crystallographic dependence in surface free energy expression:

$$\gamma = \frac{U_s - TS_s}{A(hkl)}. \tag{2.12}$$

Besides the dependence with crystallographic orientation, it seems intuitive to assume a dependence with the preparation conditions since the surface will be stable for a particular state of pressure and temperature. One can derive such a dependence naturally if we start the discussion of surface formation in the chemical potential viewpoint, as will be regarded in the next part.

Chemical potential and its influence on surface stability

The chemical potential can be defined as the derivative of the Gibbs free enthalpy for a given phase with respect to the number of particles of type i, i.e :

$$\mu_i = \left(\frac{\partial G}{\partial N_i}\right)_{p,T}. \tag{2.13}$$

Even without knowledge of the particular value μ_i, one can highlight the role of preparations conditions in the equilibrium state of a system [22]. In view of this, consider the formation of an AB compound. Its bulk chemical potential can be represented in terms of the particular $\{A, B\}$ bulk chemical potential plus the heat of formation ΔH_f^{AB} of such a structure:

$$\mu_{AB}^{bulk} = \mu_A^{bulk} + \mu_B^{bulk} - \Delta H_f^{AB}. \tag{2.14}$$

In equilibrium, the particular chemical potential μ_i $(i = A, B)$ at the outermost layers (the surface) must be equal to the bulk chemical potential, i.e:

$$\mu_A + \mu_B = \mu_{AB}^{bulk}. \tag{2.15}$$

In this scenario, each particular chemical potential is restricted to its correspondent bulk chemical potential:

$$\mu_i \leq \mu_i^{bulk}. \tag{2.16}$$

Hence variations of the preparation conditions can be represented by the deviations of the particular chemical potential μ_i from the bulk values [22]:

$$\Delta\mu_i = \mu_i - \mu_i^{bulk}. \tag{2.17}$$

By combining (2.16) and (2.17) it follows that:

$$(\mu_A - \mu_A^{bulk}) + (\mu_B - \mu_B^{bulk}) = -\Delta H_f^{AB}. \tag{2.18}$$

Then,

$$\Delta\mu_A + \Delta\mu_B = -\Delta H_f^{AB}. \tag{2.19}$$

Hence one can determine a lower and upper bounds for the variation of each μ_i:

$$-\Delta H_f^{AB} \leq \Delta\mu_i \leq 0 \tag{2.20}$$

Equation (2.20) reflects the equilibrium phase for particular preparation conditions. If $\mu_i = 0$, the surface is in equilibrium with the condensed bulk phase. Instead, $\mu_i < 0$ means that the surface is in equilibrium with the gaseous phase [22].

The surface free energy will be minimized for a given chemical potential, that is, for a given preparation condition. The explicit dependence can be obtained by expressing the gran potential $\Omega = \gamma A$ as function of the chemical potential variation, as follow:

$$\Omega(\Delta\mu_i) = E(N_A, N_{B)} - \mu_{AB}^{bulk} N_J - \mu_i^{bulk}(N_A - N_B) - \Delta\mu_i(N_A - N_B). \tag{2.21}$$

In (2.21) $i = \{A, B\}$, $j = \{B, A\}$, and N_A N_B are the number of particles of species A and B at the surface, respectively. One can illustrate the relevance of p and T from a microscopic point of view by discussing the adsorption process. Although such an issue is not part of the results covering in this work, it is worth extending some comments on it.

In this context, it is convenient to invoke the gran canonical ensemble, and then describe the whole system with the grand partition function Ξ:

$$\Xi = \sum_i Z_{i,s} e^{-\beta(E_i - \mu_s N_i)}. \tag{2.22}$$

In (2.22) $Z_{i,s}$ takes into account the contributions from the vibrational motion at the i-th site. If $i = 0$, the site is empty, then $N_0 = E_0 = 0$. Otherwise, if $i = 1$, the site is full and $N_1 = 1$, $E_1 = -\epsilon$. In absence of particles at the i-th site, the vibrational motion can be neglected, then $Z_{0,s} = 0$. Otherwise, it must be taken into account, i.e , $Z_{1,s} = Z_s$. Therefore with such assumptions, the grand partition function can be expressed as follow:

$$\Xi = 1 + z_s e^{\beta(\epsilon + \mu_s)}. \tag{2.23}$$

The average occupation per site is given in terms of the grand potential $\Omega = -k_b T \ln(\Xi)$ as:

$$\theta = \frac{N}{N_s} = -\left(\frac{\partial\Omega}{\partial\mu_s}\right)_{T,V}, \tag{2.24}$$

Hence one reads that:

$$\theta = \frac{Z_s e^{\beta(\epsilon+\mu_s)}}{1 + e^{-\beta(\epsilon+\mu_s)}}. \tag{2.25}$$

Thus solving for μ_s it follows that:

$$\mu_s = -\epsilon + k_b T Ln\left(\frac{\theta}{(1-\theta)z_s}\right). \tag{2.26}$$

Then comparing with the well-known bulk chemical potential μ_b

$$\mu_b = k_b T Ln\left(\frac{p}{k_b T}\lambda^3\right), \tag{2.27}$$

one obtains the *Langmuir* adsorption isotherm:

$$p = e^{-\beta\epsilon}\frac{\theta}{1-\theta}\frac{k_b T}{z_s \lambda^3}. \tag{2.28}$$

Historically, these intensive parameters have been pointed out as crucial for geometrical and electronic modifications of some widely investigated semiconductors, as Si and Rutile (TiO_2). Regarded to Silicon, the temperature has been revealed to drives a famous surface reconstruction: from (1 x 1) to a (7 x 7) superstructure, as demonstrated from LEED experiments carried out by [28]. On TiO_2 surface, high temperature, and low oxygen pressure imply the formation of point cation defects, as reported by [29]. Such defects are responsible to promote a significant broadening of Ti core level peaks towards lower binding energies in XPS experiments. Not surprisingly, both parameters temperature and defects play a fundamental role on surface stability and geometrical aspects in spharelite structure. The state of the art regarding research in these fields will be discussed next.

2.5 An overview on zinc sulfide investigations

Since we have discussed the main concepts regarded to defects in semiconductors and the environment dependence on the surface stability, we aimed in this section to rationalize such topics with the current state-of-the-art on ZnS investigations.

ZnS-WZ, nanobelts, and other ZnS-nanostructures will be mentioned, nevertheless, of particular interest in this research, investigations on bulk and surface on ZB-ZnS will be greater emphasized. The reader can achieves a suitable review of other ZnS nanostructure in [30].

Defects in ZnS

Regarding the doping process in ZnS structure, two main classes have been

widely explored: extrinsic doping by means of transition metal incorporation, and the vacancy formation by the removal of Zn (S) species in the zinc blende structure. Both kinds of defects might be responsible for dramatic modifications in electronic structure, optical absorption, and water adsorption either at bulk or surface level [31, 32]. However, how to identify which material should be incorporated on ZnS structure? A suitable strategy is the total energy calculation, as performed by *Kurnia*, which replace one Zn atom by a transition metal element. (Tm-doping). In this context, the enthalpy of formation is expressed as follow [33]:

$$\Delta E_f = \left(E_{Tm-doping} + \mu_{Zn}\right) - \left(E_{pristine} + \mu_{Tm-doping}\right). \tag{2.29}$$

Here $E_{Tm-doping}$ and $E_{pristine}$ are the total energy of the modelled ZnS structure with a transition metal incorporation and the total energy of the structure without modifications, respectively. The chemical potential of Zn and of the incorporated transition metal are taken into account by μ_{Zn} and $\mu_{Tm-doping}$. In this context, the author has calculated such an energy formation as function of the volume strain, and within this methodology promising candidates to be incorporated into ZnS lattice will be those that have less energy for a given volume strain. From figure 2 in [33], it is clear that manganese (Mn), copper (Cu), and cobalt (Co) are some of which attend this indispensable criterion. Indeed, these materials have driven interesting transformations on the electrical properties of ZnS, with particular emphasis on the band gap reduction: from 3.8 to 2.1 eV. This result has been pointed out for several authors as very promising for applications in catalysis physics [33].

Further to the calculations reported by *Kurnia*, several works have been attempting to understand the degree of influence of substitutional impurities on ZnS properties. For instance, *Huang and co-workers* evaluated the effect of Pb-substitutional atoms in ZnS structure [34]. Such an investigation showed that in addition to the band gap reduction, Pb states increase the absorption coefficient at different ranges rising from the ultraviolet to the visible region [34].

D'amico and co-workers have investigated the effect of aluminium (Al) and copper doping at ZnS structure in both phase, zinc blende and wurtzite. Peculiar results was found in the zinc blende structure. $Cu_{Zn} - ZnS$(i.e, ZnS structure with one zinc atom replaced by one Cu specimen) induces defect states in the pristine ZnS band gap close to the valence band maximum (VBM). In addition, these states derived from s-d hybridization, reduce the hole effective mass. This result suggests a Cu-doped ZnS as a p-type candidate semiconductor, which in terms of coast, is a very interesting finding. Conversely, Al does not induce the

formation of defect states. It donates its 3p electron to the ZnS conduction band without remarkable changes in the shape and curvature of the conduction band minimum (CBM) [35].

The later result is in contrast to the first-principles calculations reported by *Hoang and co-workers*. These authors shown shallow levels in the ZnS structure when Zn atoms are replaced by Al atoms. In addition, the levels induced from Cu_{Zn} doped lies near to the middle of the ZnS gap, then suggesting a deep level character [36]. Although such a discrepancy - that has not been explained in details yet - must be emphasized an important result regarded to the optical response of ZnS structure: The isolated Cu_{Zn} is the source of green luminescence finding in Cu-doped ZnS, as experimentally expected [37]. Nevertheless, in the presence of other dopants such as Al, only at lower Cu concentrations the green luminescence is achieved. Otherwise, the dopant-dopant interaction leads a transition from green to blue luminescence [36].

Besides the impacts on electronic and optical properties of bulk ZnS, substitutional impurities have playing an interesting role in the interaction of ZnS surface with water molecules, as discussed by [38]. The authors have suggested that the pristine ZnS surface is more hydrophilic than the Cu-activated one. Such results were evidenced by means of adsorption Energy E_{ads} calculation of H_20 molecules at spharelite surface, given by [38]:

$$E_{ads} = E_{H_2O} - (E_{adsorbate} + E_{slab}), \tag{2.30}$$

where E_{H_2O} is the energy of water molecule, and $E_{adsorbate}$, E_{slab} are the energies of the ZnS slab in the presence and in absence of water adsorption, respectively. In this scenario, the authors reported that the adsorption energy on the ZnS surface is $-53\ kJ/mol$, whereas on Cu-activated one is $-36.9\ kJ/mol$. Since the higher negative E_{ads} the higher water adsorption, then such findings reveal that Cu incorporation in ZnS decreases its hydrophilic behavior [38].

Intrinsic doping in sphalerite has been also widely explored. Before understanding the effect of native defects in ZnS structure, it is convenient to evaluate the energy required to achieve both type of defects, cationic (V_{Zn}) and anionic (V_S). The most favorable vacancy atom will be those which require a less amount of energy to be removed. Considering a pristine ZnS structure, the formation energy E_{form} might be calculated as follow [39]:

$$E_{form} = E_{V_A} - (E_{pristine} + \mu_A). \tag{2.31}$$

From *Sahraei and Laraghi*, one can inspect that the intrinsic defects play an important role on affinity of amino acids species [40]. The authors have performed first-principles calculations at different conditions: With sulfur (zinc) vacancies and defect-free surface. In the defectiveness structure, the Alamina affinity was more stable than in the ideal surface with an energy difference at about $55 kcal/Mol$ [40]. Moreover, the same authors have scrutinized the importance of intrinsic vacancies on ZnS surface in the water interaction. By first-principles calculations, different effects on local surface wettability was found: whereas a sulfur-deficient ZnS surface has an interaction energy $E_{int} = -21.96\ kcal/mol$ the surface with higher uncoordinated sulfur species, obtaining by removing Zn species, has $E_{int} = -33.22\ kcal$, thus indicating that vacancy of Zinc species increases the hidrophilicity of ZnS surface in comparison with a sulfur-defectiveness one [41]. Cation vacancy influencing the role of interaction with particles and molecules is not a result restricted to ZnS in the zinc blende phase. Recently, *Pang and co-workers* have conducted a research which aimed to investigate the effect of cation vacancy on ZnS-WZ surface [42]. Their first-principles calculations have shown that vacancy sites induce electronic states of higher density than the pristine surface and it seems to be responsible for driving photo-excited electrons to adsorbates with higher efficiency, hence benefiting the CO_2 reduction on ZnS-WZ surface [42]. *Yost et al.* have prepared quantum dots by a wet chemical method. In their research, the authors aimed to understanding the effect of Mn doping on cadmium (Cd) and ZnS quantum dots. A reduction in the electronic band gap under Mn-incorporation was evidenced by them from scanning tunneling spectroscopy. In addition, in ZnS quantum dots, a band shift toward higher bias was noted. This last finding is addressed to the hole doping mechanism obtained by the formation of Zn point-vacancy [43].

Geometrical aspects of ZnS structure have been also widely investigated. For instance, theoretical models proposed from tight binding calculations suggest that atomic displacements drive the relaxation process and induce surface states in the gap. Another commonly reported geometrical modification is derived by intrinsic defects, as detailed by *Wright* from force-field simulations [23]. The author has pointed out that the removal of Zn atoms can break out the translation symmetry hence deriving a geometrical reconstruction. According to him, this reconstruction process is expected to occur along [110] direction. However, an experimental realization that certifies this expectation for ZnS surface remains scarce.

The role of environment conditions on ZnS structure

In addition to defects, thermodynamics aspects also play a crucial role on several properties of ZnS structures. For instance, *Zakerian and Kafashan* grown ZnS thin films on (ITO) substrate, and investigate its properties by means of different techniques, such as X-ray diffraction (XRD) and photoluminescence (PL) [44]. The authors aimed to relate the impacts of the annealing temperature on the morphology of such structures. It was shown an increase of the cristalinity and a structural change on the crystallites, from zinc blende to wurtzite [44].

Shan and co-workers have prepared ZnS thin films by chemical deposition followed by thermal annealing and have noted that the annealed films have more cristalinity compared to the *as-deposited* structure. Moreover, when heated on sulfur atmosphere, such films have enhanced its transmittance and also decreased their band gap [45]. Furthermore, annealing temperature also drives an enhancement on the optical absorption of ZnS, as pointed out by *Choi and co-workers* [46]. The kind of structure is another parameter which is influenced by the temperature, as revealed by *Gode*. The author have synthesized ZnS thin films on glass substrate by chemical bath deposition. Such films in absence of annealing were found in an amorphous structure, whereas post annealing up to $500°C$ polymorphic structures were observed [47]. On the formation of others kind of ZnS nanostructures, such as nanorods, nanowires, and nano-sheets the temperature also plays a dominant role, as discussed by *Fang and co-workers*. According to them, it may be possible to obtain ZnS nanostructures with a specific morphology by controlling the reaction temperature [48].

Besides the impacts on morphology and size of ZnS nanostructures, temperature control plays a crucial role in the stoichiometric composition of ZnS/ZnO heterostructures. For instance, according to *Lonkar, Pilai, and Al Hasan*, which have synthesized ZnS-ZnO/graphene nano-photocalysist for the first time, the most efficient behavior of this nanostructures occur by controlling the oxidation of ZnS species. This process is achieved due to the reduced graphene oxide (GO), which offers more oxygenated species in order to oxidize the ZnS. However the increase in the amount of GO is only possible due to a controllable oxidative thermal treatment [49].

Impacts of temperature on the dimensionality of ZnS thin film was reported by *Zhang and co-workers* [50]. Their findings revealed an inverse relation between thin thickness and temperature. At high temperatures, the thin crystallinity is enhanced by decreasing the film thickness. Conversely, if thicker films are prepared, then low temperatures are required. In addition, the authors reported

that at higher temperatures, layer-by-layer ZnS thin films are accompanied by island formation [50]. In addition, modification in the ZnS gap was investigated as function of temperature. *Yan,ling and Zang* shown a increase on the band gap when ZnS thin films were heated up at $633K$ [51]. A similar finding was observed on N-doped ZnS nanoribbons obtained from the CVD method by *Yuan and co-workers*. The conductivity of the as-synthesized nanobelts seems to be enhanced by 100 times upon annealing at high temperature, also increasing the hole mobility [52]. In contrast, *Patel* asserts the ZnS band gap tends to increase as high as the annealing temperature [53]. Some divergence could be speculated as effect of substrate or film purity.

The substrate interaction has been reported as a crucial parameter in the geometrical aspects of ZnS surface. Recently, *Deng et al.* have showed that whereas weak Van der Waals interaction is dominant in ZnO/Au system, in ZnS/Au a charge transfer takes place [54]. In addition, the authors pointed out that at low dimensionality, the degree of material-substrate interaction could drive distinctive characteristics in comparison to the pristine bulk structure [54]. In the particular case of ZnS thin films grown on Au (111), an unreconstructed structure was expected. Nevertheless the unit cell measured from STM images are $\sqrt{3}$ and 3 times the ideal zinc blende structure, then strongly indicating a surface reconstruction [54].

In summary, much efforts in view of the understanding of electronic and geometrical properties of ZnS structure have been performed. However, there is a lack of knowledge of which are the key factors driving modifications on its surface properties, and an unequivocal unveiling of the effect of such modifications still unclear. In search of this, it is recommended to work with ZnS single crystals. Due to its high purity, surface modifications can be directly addressed to the exact precursor agent, which in this work is speculated to the preparation conditions (especially the annealing temperature). The degree of influence on both ZnS surface arrangement and composition will be derived by XPS and LEED experiments. In addition, some theoretical speculations will be indirectly evaluated from density function theory calculations. These topics will be discussed henceforth in chapter 3.

Chapter 3

Experimental Methodology

3.1 X-ray Photoelectron Spectroscopy

XPS history has started at the end of the 19th century with the Hertz experiment, which demonstrated that electrons can be ejected out from a surface by a photon incidence. *Einstein*, in 1905, supported the development in this field by introducing a mathematical description of this phenomenon, which led him to the Nobel prize award in 1921. Although in 1907 *Innes* has reported the measurement of the kinetic energy of photoelectrons excited by an X-ray tube with a Platinum anode, only in 1951 a methodical analysis of such a process was obtained, derived by Steinhardt and Serfass investigations [55]. These efforts have culminated, in 1956, in the first photoelectron system developed by *Kai Siegbahn* at Uppsala in 1956 [1] [56].

Chemical environment investigation was indeed the first proposed model for XPS applications, making such a technique known as Electron Spectroscopy for Chemical Analysis (ESCA) at its beginning. Nowadays, XPS is one of the most employed techniques in surface science investigations, being applied beyond the initial chemical analysis purpose [57]. In this section, we will describe the foundations of the photoelectric process (from quantum mechanical viewpoint) and general aspects of an XPS spectrum.

3.1.1 Theoretical point of view

XPS is characterized by the emission of electrons from an initial state i with wave functions ψ_i to the final state f with wave function ψ_f due to the incidence of photons with energy $\hbar\omega$ originated by an x-ray source.

[1] He was also honored with the Physics Nobel prize 27 years later

The excitation promoted by the photon field can be treated by means of time dependent perturbation theory [20]. In this context, for a small perturbation Δ, the transition probability per unit of time $w_{i,f}$ between the initial and final state is governed by the well-known Fermi's golden rule [58]:

$$w_{i,f} \propto \frac{2\pi}{\hbar}\langle\psi_{E_f}|\Delta|\psi_{E_i}\rangle\delta(E_f - E_i - \hbar\omega). \tag{3.1}$$

In the most general form, the perturbation term can be written in terms of the scalar and vector potential, ϕ and $\mathbf{A}$, respectively [58]:

$$\Delta = \frac{e}{2mc}\left(\mathbf{A}\cdot\mathbf{p} + \mathbf{p}\cdot\mathbf{A}\right) - e\phi + \frac{e^2}{2mc^2}\mathbf{A}\cdot\mathbf{A}, \tag{3.2}$$

where $\mathbf{p} = i\hbar\nabla$ is the momentum operator. By neglecting the two photon process (account on the last term of (3.2)) and assuming $\nabla\cdot\mathbf{A} = 0$ due to the translation invariance, one retains:

$$\Delta = \frac{e}{mc}\mathbf{A}\cdot\mathbf{p}, \tag{3.3}$$

where in addition to the arguments above, the commutation relation was employed to obtain (3.3) .

The commutation relation also implies the following equivalence:

$$\langle\psi_{E_f}|\mathbf{A}\cdot\mathbf{p}|\psi_{E_i}\rangle \propto \langle\psi_{E_f}|\mathbf{A}\cdot\mathbf{r}|\psi_{E_i}\rangle \tag{3.4}$$

Since $\mathbf{A}$ is constant over the interaction volume, equation (3.4) allows us to write the matrix elements in terms of $\mathbf{r}$. Consider the system under investigation composed by N electrons. One of those in the final state will be find with a kinetic energy K. Assuming that this electron was ejected from the orbital κ, the initial state can be written as a product of the orbital from which the electron is excited $\phi_{i,\kappa}$, and the wave functions of the remain (N-1) electrons $\psi_i^{\kappa}(N-1)$:

$$\psi_i(N) = C\phi_{i,\kappa}\psi_i^{\kappa}(N-1). \tag{3.5}$$

In the same way, the final state ψ_f reads as:

$$\psi_f = C\phi_{f,E_K}\psi_f^{\kappa}(N-1). \tag{3.6}$$

Therefore from (3.5) and (3.6) the transition matrix elements $M_{i,f}$ can be

written as follow [21]:

$$M_{i,f} = \langle \psi_f | \mathbf{r} | \psi_i \rangle = \langle \phi_{f,E_K} | \mathbf{r} | \phi_{i,\kappa} \rangle \langle \psi_f^{\kappa}(N-1) | \psi_i^{\kappa}(N-1) \rangle \quad . \tag{3.7}$$

Now consider that there are ϵ excited states with the wave function $\psi_{f,\epsilon}^{\kappa}(N-1)$ and energy $E_\epsilon(N-1)$. In this sense, $M_{i,f}$ must be calculated by summing over all ϵ possible excited states, hence

$$M_{i,f} = \langle \phi_{f,E_K} | \mathbf{r} | \phi_{i,\kappa} \rangle \sum_{\epsilon} c_\epsilon, \tag{3.8}$$

where

$$c_\epsilon = \langle \psi_{f,\epsilon}^{\kappa}(N-1) | \psi_i^{\kappa}(N) \rangle \quad . \tag{3.9}$$

Thus $|c_\epsilon|^2$ is the probability of the removal of an electron from orbital ϕ_κ of the N electron ground state leaves the system in the excited states ϵ of N-1 electrons. Its sum corresponds to the well-know spectral function A and is responsible for the line shape of the spectrum.

With such arguments, it is not surprisingly that the photocurrent I_{PES} measured in photoelectron spectroscopy (PES) experiments is written as follow [58]:

$$I_{PES} \propto \sum_{i,f,\kappa} |\langle \phi_{f,E_K} | \mathbf{r} | \phi_{i,\kappa} \rangle|^2 A \delta(E_f + E_\epsilon - E_0(N) - \hbar\omega) \quad . \tag{3.10}$$

In the non-interacting scheme, the spectral function reflects solely the occupied density of states. Then in the "homogeneous broadening" situation, the peak components of the spectrum should have a Lorentzian-like shape. However, this is only an idealization. In the real scenario, we cannot neglect inelastic scattering, electron-electron interactions, and the collective oscillations contributions, for instance. In the next section, we shall explore both the physical meaning and the influence on the final structure of such beyond-elastic process interactions from a qualitative viewpoint.

3.1.2 Qualitative analysis of XPS spectra

Figure 3.1 gives a schematic illustration of relevant energy terms in XPS. The process can be divided into three steps. Firstly, photons provided by an x-ray source reach the sample with a characteristic energy $\hbar\omega$. In the sequence, these photons will interact with the electrons -bonded in the solid with a binding energy E_b-. Each photon with sufficient energy to excite an electron will give rises to a photoelectron-hole pair. In the final stage the electron will be ejected to vacuum

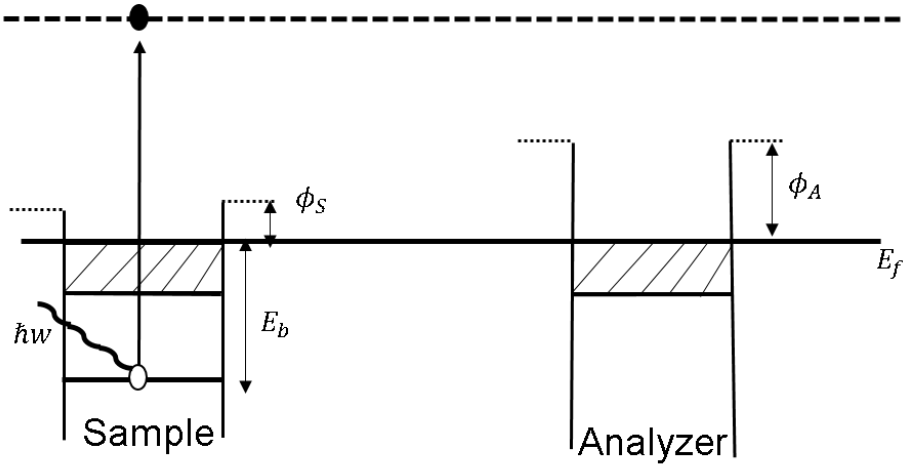

Figure 3.1: Schematic illustration of relevant energy terms in XPS *Adapted from [58]*

level with a characteristic kinetic energy K after surmounting the work function threshold ϕ_s. This kinetic energy is expressed as follow :

$$K = \hbar\omega - E_b - \phi_A, \tag{3.11}$$

where ϕ_A is the analyser work function whose value typically ranges from 4 to 5 eV [56]. This quantity can be measured empirically with reference samples, as Silver (Ag) and Gold (Au) [2]. In this scenario, assuming analyser and sample in the same potential, as depicted in Figure 3.1, the kinetic energy of those photoelectrons can be described in the well-known form [56]:

$$K = \hbar\omega - E_b. \tag{3.12}$$

The photoelectrons are emitted from different depths d in the solid[3]. During their traveling, some of those lose their energy due to inelastic events. The mean distance that these electrons can move without inelastic loss, i.e their inelastic mean free-path (IMPF), is restricted to a few nanometers. Both elastically and inelastically ejected electrons are taken into account by the attenuation length λ [60]. This parameter governs the Beer's law, which describes the intensity I of electrons emitted from a particular depth d [60]:

$$I = I_0 exp(-d/\lambda). \tag{3.13}$$

It can be shown that about 95 percent of the electrons will escape from a depth

[2] One can measure the sample work function from XPS measurements too. However, ultra-violet spectroscopy (UPS) is most convenient for such a proposal. See [59]

[3] For convenience, depth and escape depth will be equivalents henceforth

of 3λ (for the typical kinetic energy, 10 nm or less), thereby configuring XPS as a surface-sensitive technique [60]. The escape depth can be altered by changing the takeoff angle θ, since both are related as follow:

$$d = d_0 cos(\theta), \tag{3.14}$$

where d_0 is the escape depth from normal emission. This strategy is convenient when one aims to investigate the outermost layers of a surface. For this purpose, it is strongly recommended to compare peaks that emerge almost from the same depth. On ZnS, Zn 3p and S 2p attending such a prerequisite.

We now will discuss the relevant aspects of an XPS spectrum and address the physical meaning behind the characteristic peak in the spectra. Figure 3.2 illustrate the electron path during XPS experiments

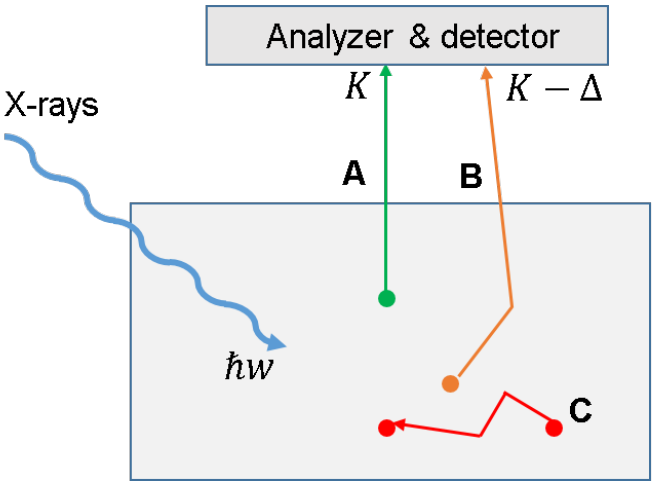

Figure 3.2: Different kind of events during the electron travel towards the analyzer *Adapted from [60].*

Elastic photoelectrons, labeled as 'A' in Figure 3.2, contribute to the main peaks in XPS spectra. Typically, such peaks are described by a convolution of Gaussian and Lorentzian (GL), mixed by a factor x [61]. For x = 100, i.e GL(100), a single Lorentzian peak is assumed, whereas GL(0) means a single Gaussian peak. On the other hand, the inelastic scattering, labeled as 'B', gives rise to the background, which can be subtracted by Linear, Shirley or Tougard background line, being the last the more robust one [62]. In addition, the own x-ray source can increase the background contribution. If non-monochromatic x-ray sources are employed, the background is accompanied by satellite peaks due to X-ray satellite lines [56]. Therefore monochromatic sources have been commonly used to gives more accurate and regular line peaks in comparison with a non-monochromatic source, as depicted in Figure 3.3. In this thesis we used a

monochromatic X-ray source. In addition, Tougaard background line, GL (80), and GL (30) were adopted for background subtraction and Zn 2p and S 2p peak fitting, respectively.

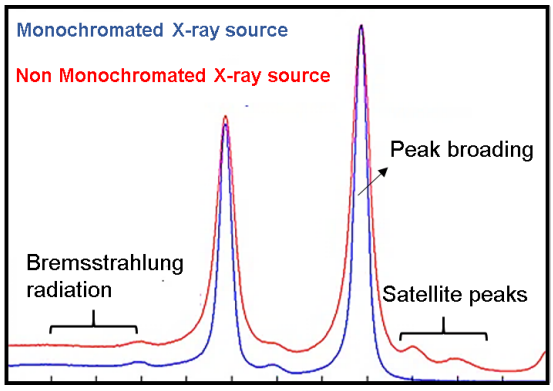

Figure 3.3: Difference between XPS spectra derived by Monochromatic and non-monochromatic x-ray source . *Adapted from [63].*

Returning to the issue regarding contributions on XPS spectra, we now will comment about the collective oscillations modes of the solid, called *plasmons*. The intrinsic plasmons arise due to the deexcitation of the photo-hole, being an intrinsic (as the name suggests) property of the photoemission process. Nonetheless, identify such an intrinsic component is not simple matter of immediate application [58]. Since these plasmons are coincident with the extrinsic ones, the relative intensities of successive plasmons must be considered. Then, as this quantity is different, one achieves an unequivocal identification, as suggested by [64]. Contrasting, extrinsic plasmons are addressed to an energy loss process. They are originated by the interaction of the photoelectron during the travel into the solid with the remaining electrons in a collective oscillation configuration, and their typically magnitude order 10 - 30 eV for bulk plasmons peaks.[4].

A remarkable component in XPS spectra also derived by the deexcitation process is the Auger peak, whose origin is illustrated in Figure 3.4. The removal of an electron from an energy level W results in a hole in this state. To compensate it, an electron from a higher energy level X will fill the previous vacancy. Therefore, the excess energy will gives rise to another electron emission, now from this X level. This is the *Auger* electron. Since this transition - labeled as A_{WXX}- depends on the binding energy of these specific levels, its kinetic energy will be independent of the x-ray source.

The rearrangement after a photoemission can also originates new components in the spectra, which is established as a *final state* effect. Typically, the loose of a

[4]Surface plasmons can also arise. Typically their binding energies is shifted by a factor $1/\sqrt{2}$ of the bulk plasmons [58]

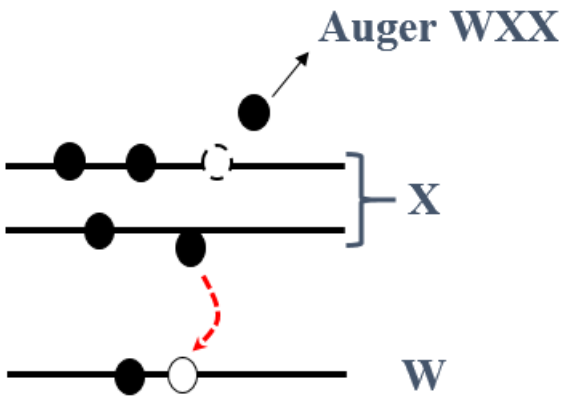

Figure 3.4: Illustration of Auger electron emission.

few eV of kinetic energy in transition metals with unpaired electrons are reflected in a new peak that lies few eV at higher binding energies in relation to the main component. This scenario illustrates the *shake-up* effect. On the other hand, the interaction of the photoelectrons with electrons in the valence band can be reflected in the spectra by the called *shake-off* effect. This effect takes place due to the loss of kinetic by the photoelectrons excited in the empty states near to the Fermi edge [57]. As consequence, an asymmetric peaks at higher binding energy in relation to the core peak results.

A physical assignment of a peak is the full-width half-maximum (FWHM). FWHM is described by three main factors: The natural width of the core-hole state, ΔE_m, related with the uncertainly principle, $\Delta E_m \Delta \propto h$, in which Δt is the core-hole life-time; The photon source dispersion, ΔE_p, and the analyser resolution, ΔE_a. With such parameters, the FWHM corresponds to [57]: $\sqrt{(\Delta E_m)^2 + (\Delta E_p)^2 + (\Delta E_a)^2)}$. Hence, it is convenient to impose constraints on the peak position and FWHM values, since if the decovolution assumes values out of the FHWM bounds then such peaks must be neglected since there is no physical meaning for it. The atomic percentage of each element in the spectra can also be determined. This purpose is achieved by dividing the peak area to the relative sensitive factor (RSF), which incorporates all the terms related to the spectrometer and the specimen, like the spectrometer transmission function and attenuation length [57]. Therefore, to compare the atomic ratio of different species, peaks with almost the same escape depth must be considered. This point will be recalled in chapter 4, herewith FWHM measurements, whose broadening may be addressed to some physical phenomena, as discussed in details in such a chapter.

3.2 Low Energy Electron Diffraction

3.2.1 Historical aspects

Owing to the wave-particle theory proposed by *L. de Broglie* in 1924 [14], electron beams reaching a crystal were expected to give rise to the diffraction pattern of the periodic lattice. The first experiment that confirmed such a hypothesis was conducted (accidentally!) by *Davison and Germer*. From this experiment, a diffraction pattern of Nickel (111) from electron incidence (with the energy around 300 eV) was revealed [65]. Although the strong research interest in this new phenomena, solely 40 years after its discovery a reproducible setup of LEED patterns was achieved, thanks to the development of a post acceleration system and a Faraday cup collection combined with advances on UHV systems.

Currently, LEED is broadly used in surface science investigations, especially on the understanding of the surface structure, with particular emphasis on the geometrical arrangement. Hereafter, we will exploit the main aspects of LEED theory starting with a brief introduction of diffraction concepts and closing the section with a model to geometrical interpretation of LEED patterns.

3.2.2 Theoretical background and analysis

Diffraction can be considered as a mapping of the reciprocal space which are connected with the real component of a system by:

$$\mathbf{a}_i \cdot \mathbf{b}_j = 2\pi\delta_{i,j}, \tag{3.15}$$

where $\mathbf{a}_i$ and $\mathbf{b}_j$ are the basis vector in the real and reciprocal space, respectively.

On the theoretical point of view, the diffraction condition arisen from *Von Laue* condition, which can be derived from kinematic theory arguments. In this sense, consider an incident wave vector $\mathbf{k}$ reaching the sample, and sequentially being scattered to a final state state with a wave vector $\mathbf{k'}$. In such a process, the transition amplitude $c_{\mathbf{k},\mathbf{k}}$, is governed by the potential $V(\mathbf{r})$ in the region that is reached by the beam such that [66]

$$c_{\mathbf{k},\mathbf{k}} = -\frac{i}{\hbar}\int d\mathbf{r}\int_0^{t'} dt'\psi_f^* V(\mathbf{r})\psi_i. \tag{3.16}$$

The potential whose describe the interaction of the particle with the solid can be written as function of an instantaneous positions $\boldsymbol{\rho}_n(t)$, which takes into

account the time independent equilibrium position (parallel to the surface), $\mathbf{r}_n$, and the displacement $\mathbf{s}_n(t)$, i.e:

$$\boldsymbol{\rho}_n(t) = \mathbf{r}_n + \mathbf{s}_n(t). \tag{3.17}$$

Such a quantity is related with the displacement in the real space $\mathbf{r}$ by the follow relation:

$$\mathbf{r} = \boldsymbol{\rho}_n(t) + \boldsymbol{\eta}, \tag{3.18}$$

where $\boldsymbol{\eta} = \boldsymbol{\eta}(r)$ is the difference of the atomic position and the instantaneous positions after the electron scattering, resulting $d\mathbf{r} = d\boldsymbol{\eta}$.

Therefore by assuming wave functions with a plane wave character, i.e

$$\psi_i = \frac{1}{\sqrt{V}} e^{i(\mathbf{k}\cdot\mathbf{r} - Et/\hbar)} \tag{3.19}$$

$$\psi_f = \frac{1}{\sqrt{V}} e^{i(\mathbf{k'}\cdot\mathbf{r} - E't/\hbar)}, \tag{3.20}$$

and combining (3.17) and (3.18) in (3.16), the amplitude probability reads as [66]:

$$c_{\mathbf{k},\mathbf{k'}}(t) = -\frac{i}{\hbar}\frac{1}{V}\sum_n \int_0^{t'} e^{i(\mathbf{k}-\mathbf{k'})\cdot(\mathbf{r}_n + \mathbf{S}_n(t))} e^{i(E-E')t/\hbar} f(\boldsymbol{\eta}), \tag{3.21}$$

being $f(\boldsymbol{\eta})$ the structure factor of the sample under consideration. By assuming small displacement $\mathbf{S}_n(t)$, one can expand the term $e^{i(\mathbf{k}-\mathbf{k'})\cdot\mathbf{S}_n(t)}$ in (3.21) as follow:

$$e^{i(\mathbf{k}-\mathbf{k'})\cdot\mathbf{S}_n(t)} = 1 - i(\mathbf{k}-\mathbf{k'})\cdot\mathbf{S}_n(t) \tag{3.22}$$

Thus the amplitude probability is given by [66]:

$$c_{\mathbf{k},\mathbf{k'}}(t) = -\frac{i}{\hbar}\frac{1}{V} f(\boldsymbol{\eta}) \sum_n e^{i(E-E')t/\hbar} \int_0^{t'} e^{i(\mathbf{k}-\mathbf{k'})\cdot\mathbf{r}_n} \left[1 - i(\mathbf{k}-\mathbf{k'})\cdot\mathbf{S}_n(t)\right] dt \tag{3.23}$$

The first term in (3.23) is addressed to the elastic process since it does not contain the vibrational amplitudes, which is taken into account by the time dependent displacement $\mathbf{S}_n(t)$ present in the second term and thus addressed to the inelastic process. The elastic scattering probability

$$W_{\mathbf{k},\mathbf{k'}} = \lim_{t\to\infty} \frac{1}{t} |c_{\mathbf{k},\mathbf{k'}}|^2, \tag{3.24}$$

has non vanishing terms only for [66]

$$\mathbf{k} - \mathbf{k'} = \mathbf{G}, \tag{3.25}$$

being $\mathbf{G}$ a reciprocal vector. This is the well-known *Von Laue* condition.

When electrons are the primary source for a diffraction experiment, their inelastic mean free path into the solid must be emphasized. Such a characteristic is not strongly dependent on the chemical status of the system. In fact,it obeys a well-known universal curve, depicted in Figure 3.5.

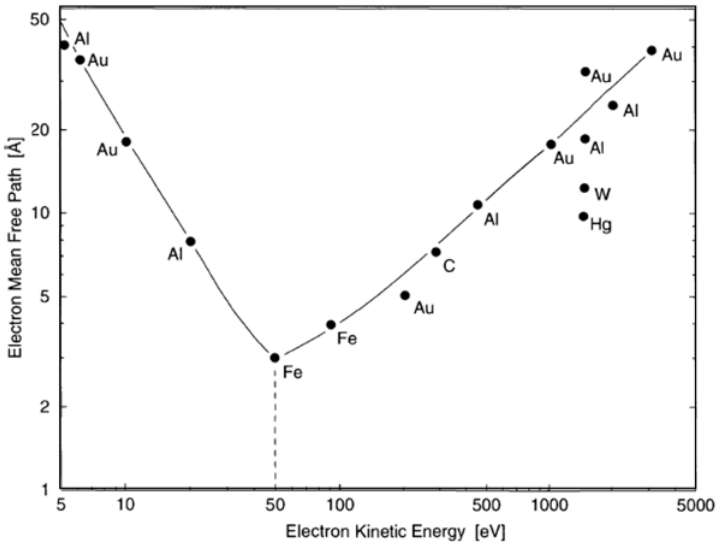

***Figure 3.5: Electron Mean free-path: The universal Curve**[66].*

In the low energy domain, ranging between $20 - 500eV$ the inelastic mean free path lies at about 5-10 Å, which turns LEED a distinguished technique for surface investigations. The elastically-scattered electrons (spots in the screen) give rise to a pattern that belongs to one of the 5 Bravais lattices [5]. Therefore, crystallographic aspects of a surface can be inferred from LEED experiments, in particular. Such lattices are illustrated in Figure 3.6.

Keeping in mind that LEED experiments derive a mapping of the surface reciprocal space, it is convenient take a bit of discussion regarded to surface notations as well as take a look to the correspondent spot configuration related to the real space geometry, as depicted in Figure 3.7.

By defining a normal vector $\mathbf{n}$ to the surface, the surface reciprocal basis $\{b_i\}, i = 1, 2$ are related with the surface real basis $\{a_i\}$ similarly as in 3-D scenario [65]:

[5] Assuming a conductive system!

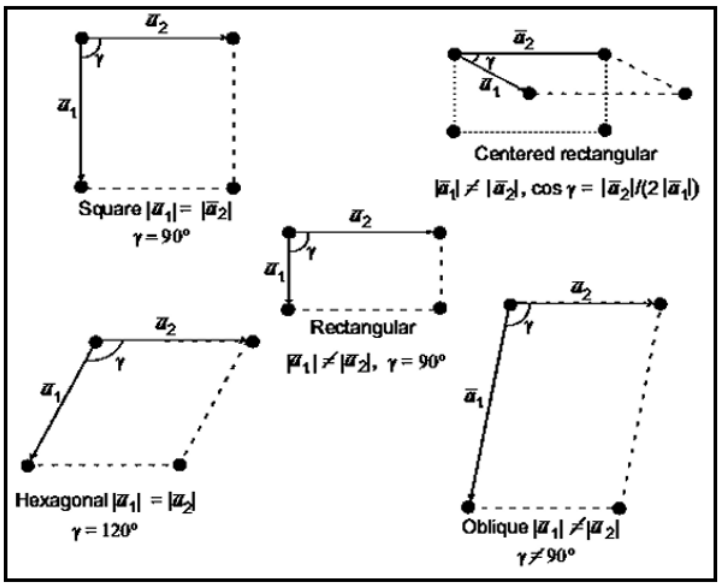

Figure 3.6: The five 2-D Bravais Lattice. *Adapted from [65].*

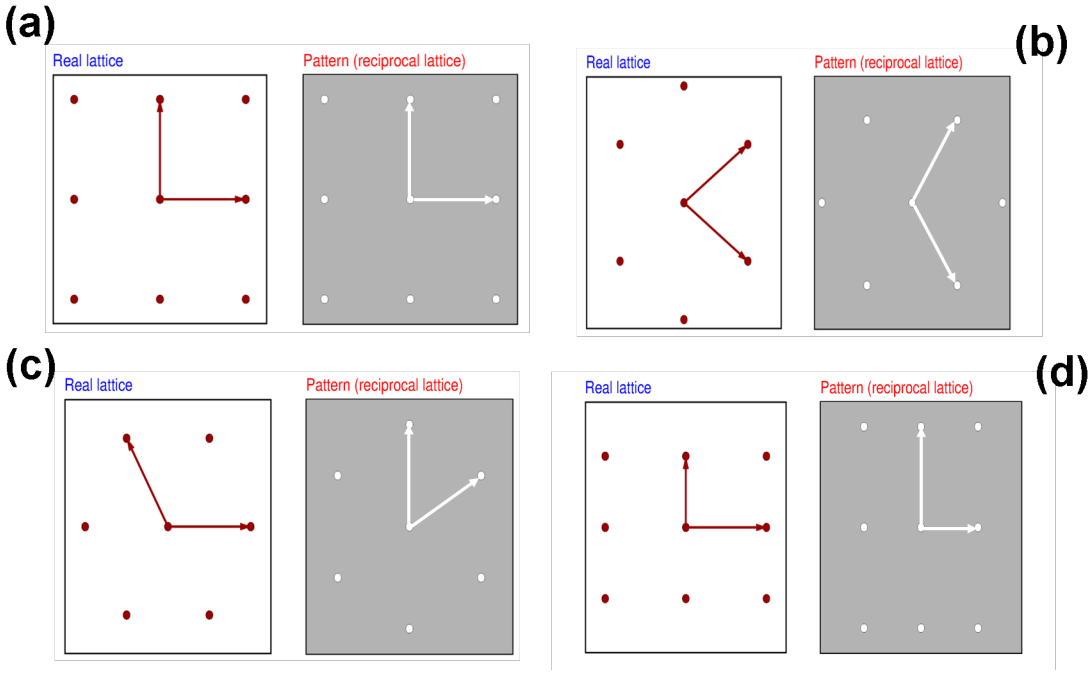

Figure 3.7: Some reciprocal lattices. *(a) Square ; (b) Centered Retangular ; (c) Hexagonal ; (d) Primitive Retangular illustrated by the author with support of LEEDpat software [67]*

$$\mathbf{b}_1 = 2\pi \frac{\mathbf{a}_2 \times \mathbf{n}}{|\mathbf{a}_1 \times \mathbf{a}_2|} \tag{3.26}$$

$$\mathbf{b}_2 = 2\pi \frac{\mathbf{n} \times \mathbf{a}_1}{|\mathbf{a}_1 \times \mathbf{a}_2|} \tag{3.27}$$

By denoting the bulk-like layers basis as $\bar{a}_i$ those primitive vectors of surface

lattice are related to them as follow [22]:

$$\mathbf{a}_i = \sum_{j=1}^{2} m_{i,j}\bar{\mathbf{a}}_j \quad , \tag{3.28}$$

where $m_{i,j}$ are the matrix elements of the 2×2 M matrix:

$$M = \begin{pmatrix} m_{11} & m_{12} \\ m_{21} & m_{22} \end{pmatrix} \quad . \tag{3.29}$$

Non-necessarily both bases will match each other. The surface unit cell length might be a multiple length of the bulk structure. Physically, this process is addressed to a translation symmetry breaking along a particular [hkl] orientation and is called surface reconstruction, as discussed in chapter 2. In addition, such a unbalance might be accomplished by a rotation of some degree in relation of the bulk basis and/or by an adsorption of a component X. Then to describe this process in a more simplified way, Wood notation must be used. From this notation, a specific structure S oriented along (hkl) plane having a symmetry $\left(\frac{|\mathbf{a}_1|}{|\bar{\mathbf{a}}_1|} \times \frac{|\mathbf{a}_2|}{|\bar{\mathbf{a}}_2|}\right)$ accompanied by both a rotation of θ degrees and an adsorption of an element X is described as:

$$S = S(hkl)\left(\frac{|\mathbf{a}_1|}{|\bar{\mathbf{a}}_1|} \times \frac{|\mathbf{a}_2|}{|\bar{\mathbf{a}}_2|}\right) R(\theta) - X \quad . \tag{3.30}$$

In eq. (3.30), the primitive unit cell is assumed implicitly. If the surface vector basis are centered instead, the notation should be reads as:

$$S = S(hkl)c\left(\frac{|\mathbf{a}_1|}{|\bar{\mathbf{a}}_1|} \times \frac{|\mathbf{a}_2|}{|\bar{\mathbf{a}}_2|}\right) R(\theta) - X \quad . \tag{3.31}$$

A geometrical interpretation of LEED experiments can be derived from the Ewald sphere. In the Ewald construction, the end of the primary-beam wave vector is positioned at the origin of the reciprocal space (0,0). Then a sphere with radius $|\mathbf{k}|$ is built, as illustrated in Figure 3.8. The Laue condition limits the points that will lie on the screen.

It is worth noting that as $\mathbf{k}$ is varied (by varying the electron energy, for example) the Ewald sphere passes through successively strong and weak regions, translated into modifications on the spots intensities in the screen. The dependence of such intensities with the source energy could be evaluated by an I-V curve, a suitable strategies commonly used in LEED experiments [65]. In this thesis, however, we will not deal with this experiment.

For a geometrical understanding of the surface properties with assistance of

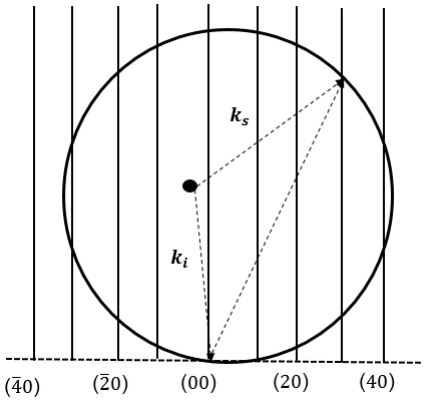

***Figure 3.8: Ewald sphere**. Adapted from [66].*

LEED experiments, a crucial result is the surface unit cell measurement. In view this, it is required an initial "calibration" with support of a standard sample, like Cu, for instance, whose LEED pattern is illustrated in Figure 3.9 [6]

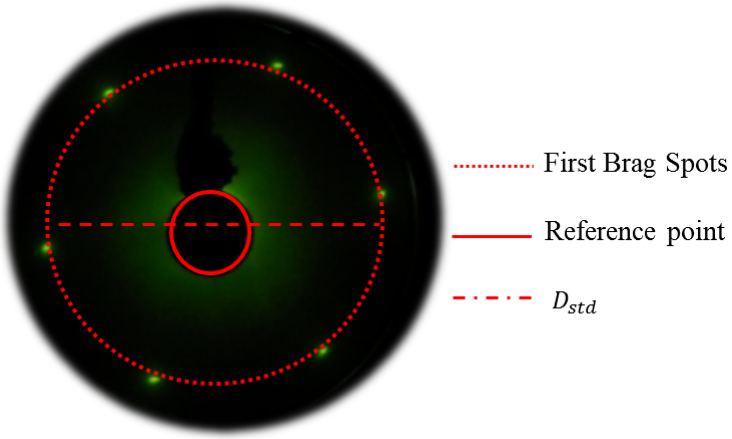

Figure 3.9: LEED pattern of Cu (111)

Standard sample, in this context, means a system with a known surface lattice parameter that can be used as reference calibration in order to estimate the lattice parameter of the surface unit cell of the sample under investigation (thin films or single crystals, for example). This task can be achieved by the following steps. Firstly, a circle of diameter D_Std containing the primaries Bragg spots is done. Sequentially, one can calibrate the distance in the screen in terms of the well-known lattice parameter a_{std} by the following relation:

$$\frac{1}{D_{std}} = a_{std}. \tag{3.32}$$

In the same vein, one applies the relation (3.32) for the particular sample under

[6] Thanks to our teammate *Astrid Alí*

investigation,

$$\frac{1}{D_{sample}} = a_{sample}, \tag{3.33}$$

where D_{sample} is the diameter of the circle that contains the primary Bragg spots of the sample whose lattice parameter a_{sample} will be evaluated. Finally, by combining the last relations the lattice parameter of a surface unit cell can be estimated by the follow statement :

$$a_{sample} = a_{std}\left(\frac{D_{std}}{D_{sample}}\right). \tag{3.34}$$

Such a strategy allowed us to calculate the lattice parameter of the ZnS single crystal [7], whose crystallographic aspects will be emphasized in chapter 4.

3.3 Experimental Setup of XPS and LEED

All XPS and LEED experiments were carried out in an Ultra High Vacuum (UHV) system (SPECS PHIBOS 150) equipped with standard surface preparation facilities. UHV conditions are mandatory in these experiments, since the presence of contaminants at the surface of the sample can drives undesirable effects as a decrease in the electron mean free path, for instance. UHV scenario is achieved with assistance of pumping technology, whose typical components are:

- *Mechanical pump*, responsible to the primary vacuum, lying in the low vacuum range, i.e, at about $10^{-2}mbar$;
- *Turbomolecular pump*,combined with mechanical pumps can yields high vacuum conditions, ranging from 10^{-7} to $10^{-9}mbar$;
- *Ionic pump*, a static pump that ionises chemically active gases and removes them from the system, enabling UHV conditions ($10^{-10}mbar$) ;
- *Titanium Sublimation pump*, another static pump that help to maintain the vacuum bellow $10^{-9} - 10^{-10}mbar$.

More information about the work process of vaccum pumps could be found elsewhere [68, 69].

[7] Keep in mind this methodology works for square lattice or thin-film growth on a metallic substrate only. In the case of a hexagonal single-crystal, a correction factor must be applied to it, one considering the distance between two non-consecutive maxima.

XPS Setup

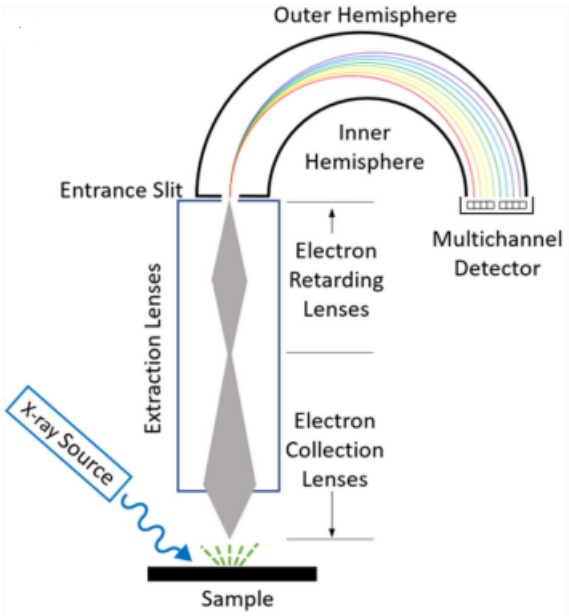

Figure 3.10: The electron path in the XPS experiments *[60]*

A basic scheme of the XPS apparatus is illustrated in figure 3.10. The photoelectrons which escape from the surface into the vacuum pass through the collection lens and are directed towards the entrance analyzer slits of the spectrometer, and are detected when reaching up the detector. The number of electrons per time unit will be counted as a function of its kinetic energy, originating an intensity vs energy plot. This plot is well known as XPS spectrum.

The electron energy analyzer is the heart of the spectrometer [57]. It can be found in cylindrical or hemispherical format. Since the last one was used in this dissertation, we will now briefly discuss its main aspects. It is formed by two concentric hemispheres of radius R_{inner} and R_{out} . Electrons with an incoming energy E_i are retarded before entering the analyzer due to a potential difference $\Delta V = V_{inner} - V_{out}$ such that

$$E_i - e\Delta V = E_0,$$

where the reduced energy E_0 is called *pass Energy*, which correspond to the electron energy traveling from the entrance to exit slit along the equipotential plane, which is defined by the medium radium R_0 as depicted in Figure 3.11 [57].

The potential different between the hemispheres must satisfy [57]:

$$e\Delta V = E_0 \left(\frac{R_{out}}{R_{inner}} - \frac{R_{inner}}{R_{out}} \right).$$

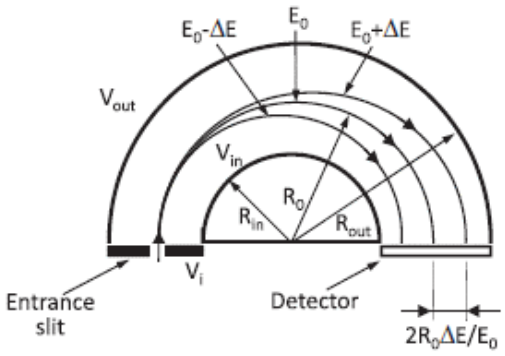

Figure 3.11: Schematic view of the hemispherical analyzer slits *[57]*

These potentials in each hemisphere are set according to the pass energy, which is responsible for the energy resolution ΔE. Typically, $\frac{\Delta E}{E_0}$ remains constant, being proportional to 2% of the resolution. Therefore, the lower pass energy is the higher is the accuracy of XPS spectra. Generally, if we are interested on general information from the spectra - that is, a *Survey* spectra-, 50 eV might be a sufficient choice to E_0. On the other hand, when we are looking for precisely and specific information, 20 eV is a suitable value.

LEED Setup

The most common apparatus of a LEED facilities consist of an electron gun E_g, whenet cylinder W_c, electrostatic grids $1^{st} - 4^{th}$, and a fluorescent screen F_s, as depicted in Figure 3.12. A commercial version follows the same scheme but may have additional components [66].

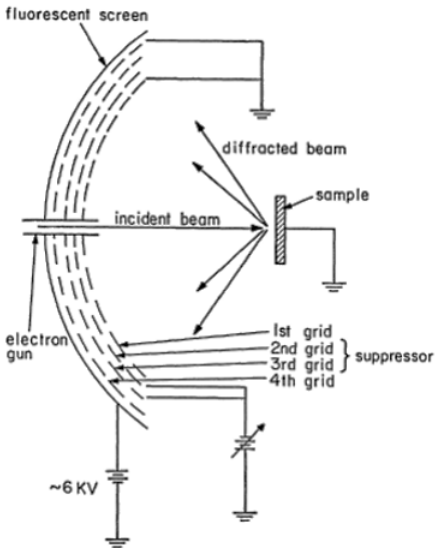

Figure 3.12: Illustration of a LEED setup *[66]*

The electron gun originates the electron beam that will pass through a Whenet cylinder, which is responsible for the initial beam collimation with an energy E'.Such an energy is determined by the potential between the cathode and the aperture between 1^{st} and 4^{th} grid, and can be controlled externally. The beam energy will be focused by others grids , and then will impinging the sample at normal incidence [66].

The elastically back-scattered electrons will be collected by a fluorescent screen, which must be biased to obtain a final acceleration of such electrons. Hence, a pattern of the reciprocal space will arise on the screen, assigned by defined spots. Those electrons which are inelastically scattered contributes to the background in the screen and commonly, in the case of a conducting system, are sufficiently suppressed by a negative bias applied in the middle grid.

3.4 Sample preparation

A clean and well-defined surface is one of the main requirement for surface sensitive techniques as XPS and LEED. Frequently, ex-situ and in-situ preparations are applied to achieve as much as possible the ideal surface conditions. Besides this, the sample mounting is of fundamental importance since depending on the electrical contact, "extrinsic" charging can results. In this work, previous to the insertion in the UHV chamber the ZnS (001) single crystal, purchased from *Mateck GmbH*, was prepared by some cycles of ultrasonic clean process. In addition, the sample was fixed on a sample holder by smalls Tantalum wires attached with spot weld, then granting a good electrical contact. In the UHV chamber, the sample was treated by several cycles of sputtering and annealing. The first process consists of the removal of some species on the surface of the sample by ion bombardment. Typically, these ions are provided from an inert gas - as Argon - which is ionized by electrons that are emitted one passing a current through the ion gun filament. Hence the ions are accelerated towards the surface by applying a high voltage in the filament. This process can eliminate some residual contaminants of the surface, however depending on its intensity can severally damage the surface, then depending on both sample structure and the ion energy, a longer time of ion bombardment must be avoided. The last process consists of the heating of the sample and is commonly addressed to the reestablishment of the surface order. In this process, the sample holder is reached up by electrons originating by a warmed filament. Since the sample is attached on the sample holder, then it will be warmed up. Care must be taken also in this process, since depending on the melting point, high temperature can results in an undesirable phase transi-

tion. In this work, the sputtering was conducted with an Ar^+ energy of 600 eV for 5 min, maintaining the pressure in the range [1 - 3] 10^{-6} mbar followed by annealing process for 10 min in a base pressure of 1.10^{-8} mbar and at distinguished temperature scenarios, which will be discussed in details in chapter 4.

3.5 Preparing a surface on DFT framework

A detailed understanding of surface properties is achieved when the experimental realizations confirm the theoretical predictions (or vice versa). In this context, first-principles calculations of surface structures are strongly recommended. A powerful method to simulate surfaces is the supercell method [70]. In this tool, one confines the region of interest into an arbitrary box, which is then infinitely repeated in a particular direction. Hence the system becomes an array of repeated periodic slabs, which are separated by a large vacuum region to prevents spurious interaction between adjacent slabs. Owing to this periodicity, one can use fast computation methods like plane-wave base sets, which turn supercell calculation of particular interest [70]. A schematic view of ZnS supercell is illustrated in Figure 3.13.

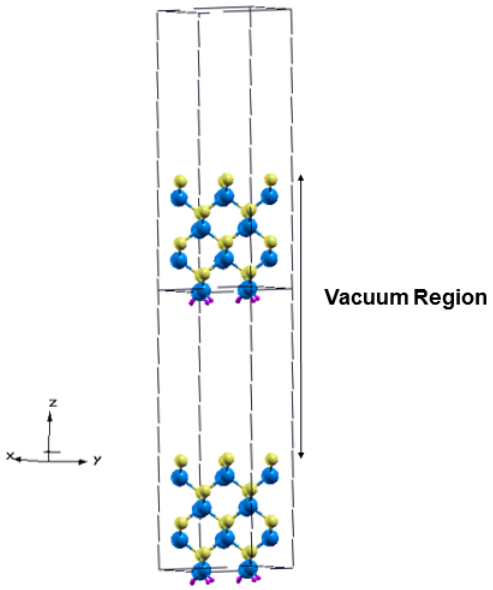

Figure 3.13: ZnS supercell. *Hydrogen atoms are denoted by purple balls. Image performed in Xcrysden software [71].*

Thereafter supercell construction, the ground state of the system is achieved after a fully or partial relaxation of the ions, whose ideal positions correspond to a minimum of energy and forces [72]. In this thesis, the ideal 1 x 1 ZnS (001) surface was simulated by 8 repeated layers of ZnS unit cell. For calculations with

vacancies (to be reported in Appendix II) the cell along $\hat{\mathbf{x}}$ and $\hat{\mathbf{y}}$ directions was duplicated, thereby configuring a 2 x 2 x 1 supercell containing 80 atoms, wherein 32 of them were zinc and sulfur atoms and the remaining 16 atoms resulted from hydrogen species that are employed to avoid fictitious contribution of the internal layers. In the surface calculations that will be reported in chapter 4, the first 4 layers were kept fixed whereas the 4 outermost layers were fully relaxed being such regions separated by 15 Åof a vacuum region. In addition to surface calculations, the bulk properties of the ZnS system were investigated. This system can be obtained from the surface slab by removing the vacuum region and the hydrogen passivation. Hence the bulk structure were modeled by 16 and 64 atoms for pristine and defectiveness slab, respectively.

Details regarding to the theoretical aspects of DFT will be discussed at the end of this thesis in Appendix I. Here, it is sufficient to summarize the main aspects employed in the simulations. All calculations were supported by the open source *Quantum Espresso* code [73]. For the exchange-correlation function, we adopted the Perdew, Burke, and Erzenrhof Generalized Gradient approximation (GGA-PBE) [74]. To describe the electron-ion interaction we used projector-augmented wave (PAW) pseudopotentials. In addition, the Brillouin zone was sampled by 6 x 6 x 1 Monkhorst-Pack k-points [75].

Chapter 4

Results and discussion

4.1 Insulating nature of ZnS and its impacts on XPS and LEED experiments

Introduction

Insulating systems frustrate some surface science investigations like XPS and LEED due to the charging effect, as discussed in chapter 1. In XPS experiments, photoelectron emission leaves the system with a positive charge status. Since this configuration is not energetically favorable, the system tends to restore its equilibrium by filling up the hole site with an electron. This electron-hole recombination mechanism is indeed ensured for systems that have a sufficient number of free electrons. However, an insulating structure cannot achieve this condition, then resulting in a strong electrostatic interaction between the ejected photoelectron and the positive charge accumulated at the surface. This interaction decreases the photoelectron kinetic energy, hence shifting all XPS components towards higher binding energies position. An interesting instrument that can circumvents this scenario is the *flood Gun*. This instrument allows electron-hole recombination by impinging low-energy electrons at the surface of the sample. By accurate controlling the beam energy and the emission current, XPS peaks are directed towards their correct binding energy positions without any loss of generality in their intrinsic properties.

The own low-energy electrons are the source of charging in LEED experiments (assuming low conductivity systems). These electrons will be accumulated at the specimen surface, which is left with a negative charge status. The electrical field resulting from these incoming electrons on the surface increase the secondary electrons contributions related to inelastic processes, modifying either the position as

the intensity of the Bragg spots. . The thermal activation process is usually employed to contour this problem. However, depending on the degree of insulating aspect, it might not be recommended, as for a strong insulating sample a large amount of thermal energy is required to increase the free electrons population. Such high temperatures might drive irreparable modifications to the surface structure .

In this section, we aim to rationalize the electronic structure of the ZnS system with the experimental findings from XPS and LEED. We will characterize the main aspects regarding the electronic structure of the ZnS, and in the sequence, evaluate the impacts of the charging effect in the experiments. Furthermore, distinguished scenarios of surface preparation with a particular interest in the annealing temperature will be compared. Closing this part, we will speculate some findings with a theoretical model to be adequately discussed next in this thesis.

Discussion

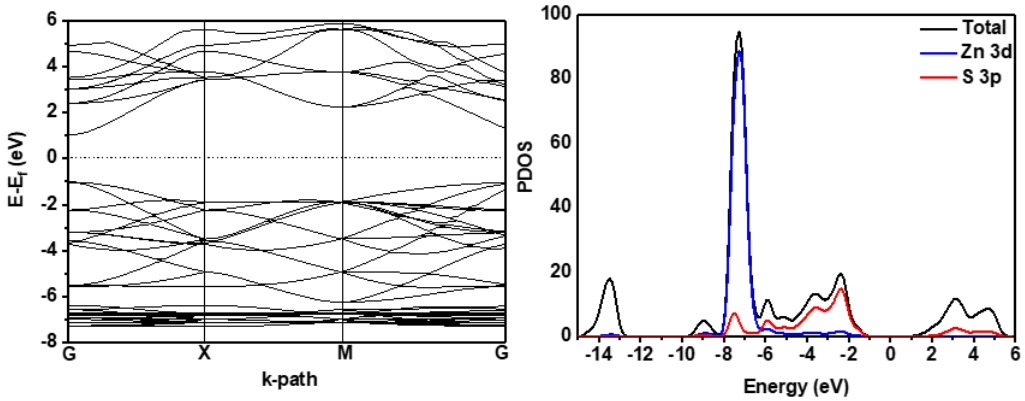

Figure 4.1: Electronic structure of ZnS bulk. *(a) band structure and (b) PDOS. The Fermi-level was shifted to 0 eV for convenience.*

Prior to start the discussion on the surface properties of the ZnS surface, it is convenient to shown the electronic structure of the bulk system, as depicted in Figure 4.1. We assumed the valence configuration as $3d^{10}4s^2$ and $3s^23p^4$ for Zn and S atoms, respectively. Figure 4.1 (a) shown the band structure of the bulk ZnS, which reveals a direct band gap of 2.2 eV. This value is pretty underestimated, however it is expected from GGA-PBE methodology, which was adopted in this study [76]. Of particular interest is the projected density of states (PDOS) plotted in Figure 4.1(b) . From the valence band and conduction band, the main

components are Zn 3d and S 3p, respectively. Although there exist some contributions from Zn 4d and S 3s, they are very small and can be neglected. The higher density of states from 3d orbital is in the middle of the valence region, whereas the S 3p states lie mainly near to the Fermi-level (shifted to 0 eV for convenience) and has a small contribution in the conduction band minimum.

The same electronic configuration must to holds at the ZnS surface. The main difference might comes from the dangling bonds, which in the case of an S-terminated slab (as we assumed here) give rise to S 3p surface states inside the forbidden zone. However in the pristine scenario, we expected a low density of such states, which means that only few states will populate the gap region above the Fermi level. Such a configuration might explains the low conductivity nature of the ZnS system.

In order to understand the correlation between this property with a disrupted LEED experiments, it is convenient recall the microscopic viewpoint of *Von Laue* condition in terms of the *matching formalism*. This formalism states that conditions for elastic events can only be fulfilled if there exists sufficient electronic states inside the crystal at the particular energy which the electrons are accelerated towards the surface [66]. In other words, we can assert that the Laue condition is valid for a particular set of energy available in the crystal, which indirectly is addressed to the number of states per unit of energy and volume, the density of states. When such a condition is not fulfilled, the inelastic events becomes dominant and then the diffraction pattern is hampered, as in the case of ZnS whose the initial LEED experiments will be regarded next.

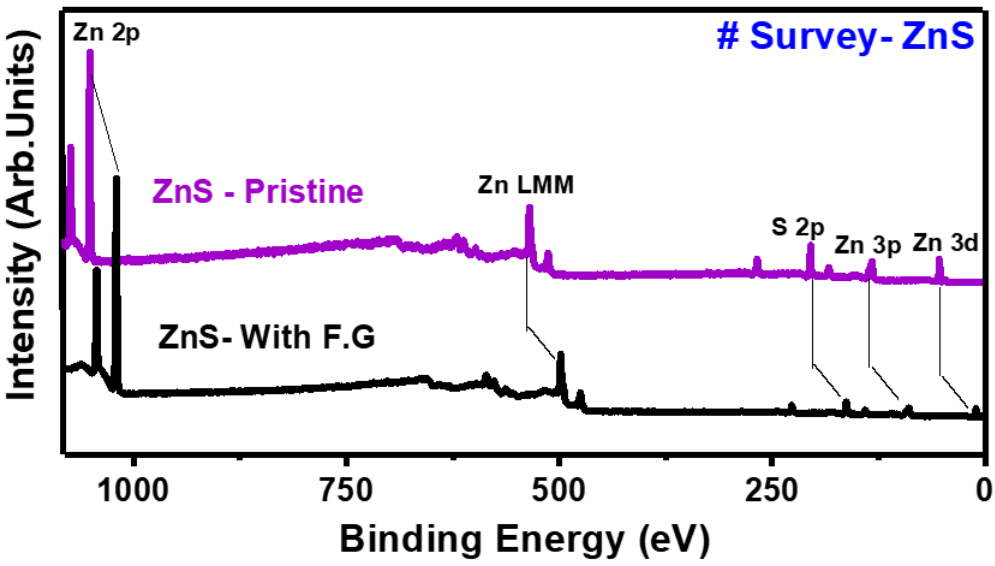

Figure 4.2: Untreated ZnS survey. *In absence (a) and with (b) flood gun assistance.*

The chemical composition and electronic behavior of the ZnS surface are de-

rived by the survey spectra depicted in Figure 4.2. The main XPS peaks are Zn 2p, Zn LMM, and S 2p, indicated in the figure. In absence of surface treatment, the main XPS components (Zn 2p, Zn LMM, and S 2p) arisen at 1074, 678 (932.30)[1], and 203 eV, respectively. Such binding energy (B.E) positions and Auger kinetic energy (See the footnote) are too much higher than those commonly reported in the literature [6]. For instance, the Zn 2p component in Zn^{+2} state binding to Sulfur anions has a binding energy ranging from $[1022 - 1022.8]eV$ as discussed by *Dengo* et.al [77], and *La Porta* and co-workers [6]. In addition,Zn LMM are emitted from ZnS system with a kinetic energy at about $988\ eV < Zn\ LMM \leq 989\ eV$ [78] . Taking the main component of the system (Zn 2p) as reference and comparing the reported binding energies with the obtained in absence of surface treatment, we can conclude that without surface preparations the photoelectrons ejected out from the insulating ZnS surface lose approximately five percent of their kinetic energy due to the charging effect. This phenomenon is translated into a large shift (at about 50 eV) of the ZnS components toward higher binding energies.

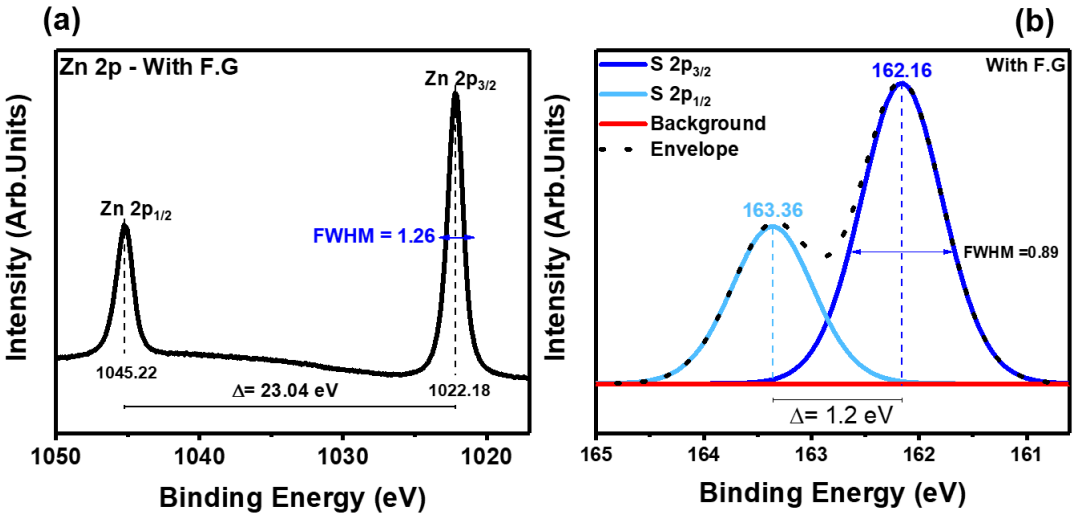

Figure 4.3: High-Resolution (H.R) spectra of the main core level peaks of the sample with flood gun: *(a) Zn 2p components and (b) S 2p components.*

This shift is pretty larger than those reported by *Barreca et.al*, which pointed out an increment of 12 eV in the binding energies position of the ZnS components [79]. In this context, the authors emphasized the need of flood Gun assistance in order to perform consistent XPS experiments carrying with insulating system such as ZnS. After several tests with such an instrument we verified 1.5 eV and $18\mu A$ as the ideal values for beam energy and and emission current, respectively. As

[1]The value inside the brackets corresponds to the kinetic energy of the Zn LMM electrons. It is common to refer to this component in such a way.

depicted in the bottom spectra (black line) of Figure 4.2- (a), flood gun assistance indeed allowed us to avoid the charging problem. In this picture Zn 2p, Zn LMM and S 2p components appear at 1022.18, 497.95 (988.71), and 162.53 eV, respectively.

It is worth noting the physical signature of the Zn 2p and S 2p components, revealed from high-resolution spectra showed in Figure 4.3-(a) and Figure 4.3-(b), respectively. Such signatures are the spin-orbit splitting Zn $2p_{3/2} - 2p_{1/2}$, S $2p_{3/2} - 2p_{1/2}$ of 23 eV and 1.2 eV, correspondingly, together with the FWHM measurements: 1.26 eV for Zn $2p_{3/2}$ and 0.89 eV for S$2p_{3/2}$. Such FHWM values are in good agreement with earlier investigation on clean metal sulfide surface, which reported values ranging from 1.2 to 1.5 eV for Zn 2p components, and 0.7 to 0.9 eV for S 2p [6]. These results will be of great relevance next in this investigation.

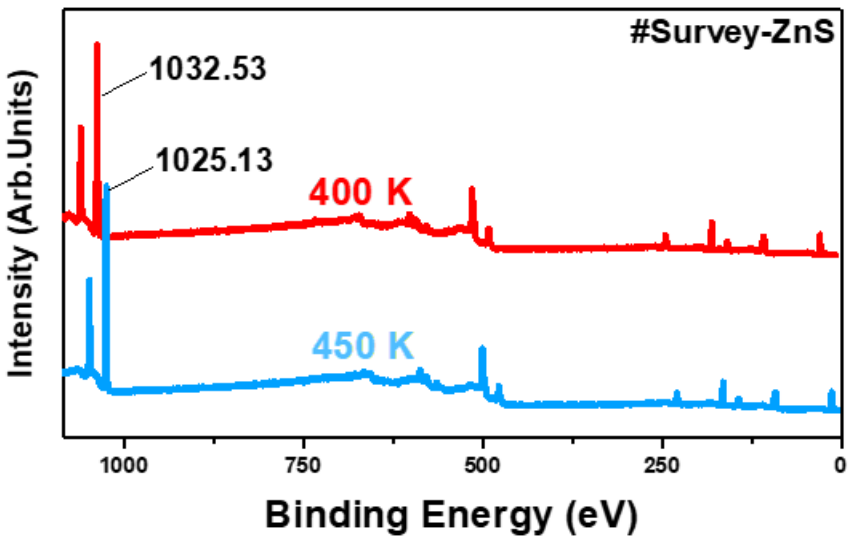

Figure 4.4: XPS surveys after the first cycles of surface preparations. *All the spectra were carried out at room temperature.*

We now turn our efforts towards converting such a system into a semiconducting structure. In view of this, thermal activation by controlled annealing cycles might be useful. We performed several cycles of ion sputtering and annealing, which at this stage was carried out at moderate temperatures: 400 K and 450 K. Figure 4.4 displays the survey spectra for each of such conditions. Initially, it can be noted a tendency of binding energy correction. This finding is highlighted by the energy shift decreasing, which post the final process is at about 4 eV (taking Zn 2p component as reference). This picture seemed promising, as this decrease in the shift is assumed to be an indication of enhancement on the surface conductivity of the ZnS structure.

Nevertheless, we observed some instability aspects in this scenario. During sequential spectra acquisition, a non-negligible increase in the shift can be noted comparing the survey spectra in Figure 4.5- (a) and (b). Furthermore, exposing the sample to atmosphere conditions and then reinsert it in the analysis chamber we noted an appreciable increase in the shift, as can be seen in Figure 4.5-(c).

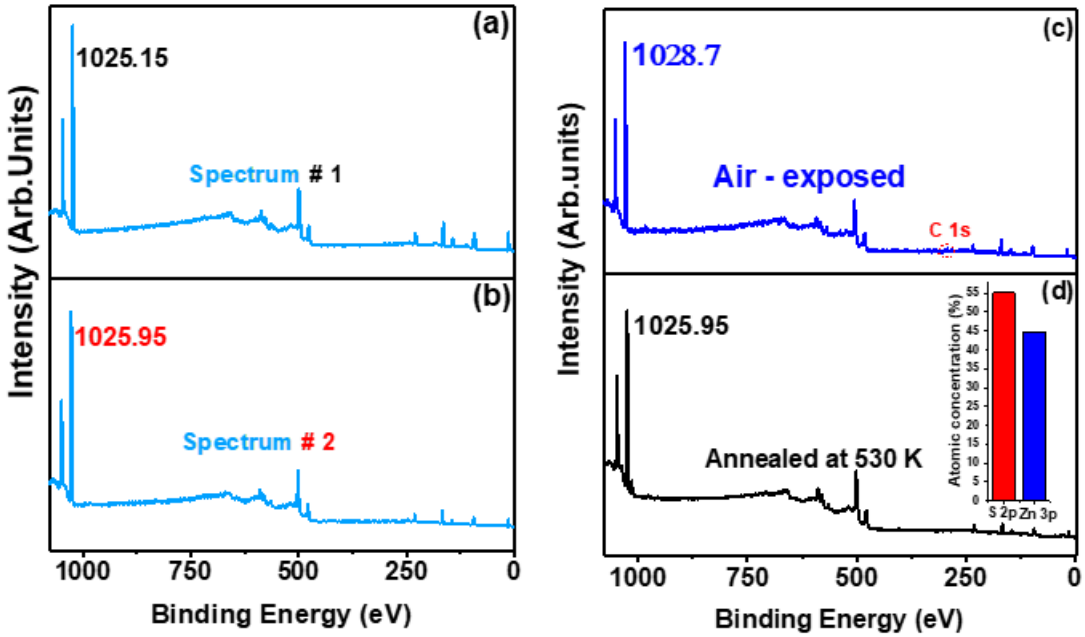

Figure 4.5: Energy shift evolution at different scenarios*. (a) and (b)Surface treatment at 450 K of annealing temperature;(c) Post a short heating at 350 K; (d) post several cycles of surface preparation carried at 530 K of annealing temperature (atomic concentration inset)*

Curiously, a new surface treatment at 530 K restored the shift of 4 eV, as grepped in Figure 4.5-(d). Evaluating the atomic concentration at this stage (Figure 4.5-(d) inset) we noted a prevalence of sulfur over zinc species. This finding suggest that the surface treatment might favors the removal of zinc atoms. Therefore we speculated that the sulfur-rich scenario is perhaps responsible to increase the ZnS conductivity, translated into a decrease in the binding energy shift. With this in mind we can rationalize about the increase in the shift when the sample was air-exposed: the atmospheric contaminants migrate to the surface and then remove such a sulfur-excess scenario, inhibiting the electron-hole recombination process. On the other hand, the unstable behavior revealed by the shift increasing during the photoelectron emission process may be explained as follow: Initially, some sulfur ions migrate to the outermost layers (which explain the apparent sulfur dominancy). This fact attributes to the ZnS surface a negative charge status, which can compensate the positive one left post the photoelectron ejection, thus warranting the shift decreasing. Nonetheless, if this segregation is inefficient to hold the electron-hole recombination, the XPS components tend to arise slightly shifted compared to the initial process, as shown in Figure 4.5-(b). Furthermore, restoring the equilibrium, the system still behaves as an insulating structure, since the ideal semiconducting scenario has not been reached yet. Such instability can support the absence of a well-defined LEED pattern even in this apparently better scenario, as depicted in Figure 4.6.

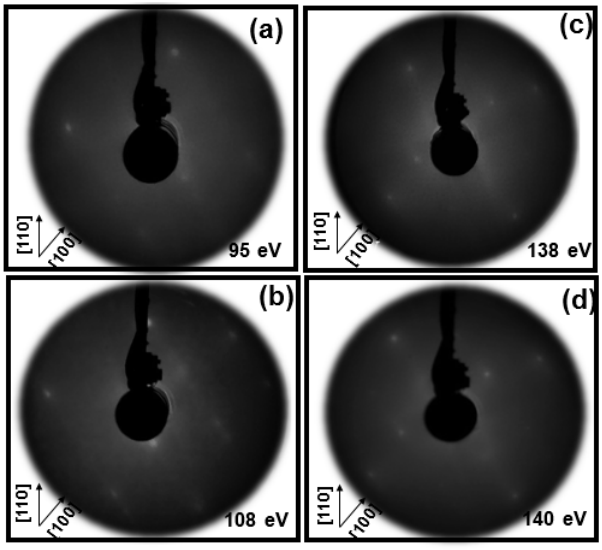

Figure 4.6: LEED patterns of the weakly treated sample *at (a) 95 eV; (b) 108 eV ; (c) 138 eV; and (d) 140 eV of electron energy. All LEED patter were adjusted to (try) enhance the image contrast*

Conclusion

In summary, in this section we presented an initial characterization of the insulating ZnS system. Its bulk and surface electronic structure were investigated by first-principles calculations. Such calculations revealed indirectly the poor conductivity of this system, which is the key property that originates the charging effect observed in XPS and LEED investigations. This phenomenon implies a large shift (at about 50 eV) on the XPS components towards high binding energy positions. In addition, this charging process implies high background contributions on LEED experiments, then unable any geometrical assumptions upon ZnS surface. In view to solve this problem, an initial surface treatment at moderate thermal annealing conditions was employed . Although we noted a large shift decreasing on XPS components, these particular conditions have been revealed insufficient to achieve the ideal scenario of surface conductivity. Nevertheless, such a strategy shown two main points that must be highlighted:

1. The surface treatment in the ZnS system might gives rise a sulfur-rich surface.

2. The sulfur-rich surface scenario might be responsible to decrease the charging

These points are inspirational to proceed with high-intense surface treatment, especially at higher annealing temperatures. This scenario might be a crucial step forward in the conversion of the insulating nature of the ZnS system into a semiconducting structure.

4.2 Converting the ZnS surface into a semiconducting system

Introduction

Based on the previous findings, we can speculate that higher annealing temperatures are indeed recommended since such conditions favor S dominancy through the removal of Zn species, which apparently decrease the charging. If confirmed, by increasing the surface treatment we might be able to carry XPS experiments and note the XPS components appearing in the correct binding energy position, even in absence of flood gun assistance. It is worth remember that the removal of some species generally are unstable, which means that the remaining atoms must to finding a new minimum of surface energy in terms of the ideal position into the

lattice. Sometimes this process can induces a symmetry breaking along a particular direction, as mentioned in chapter 2, resulting in a surface reconstruction.

It seems intuitive expects some geometrical modifications in the final cation-defectiveness ZnS surface. Moreover, zinc blend structures commonly reveals surface reconstruction along the [110] direction. Nonetheless, these expectations have not been confirmed experimentally yet. In the case of an ideal non-charging scenario, LEED experiments might reveals such assumptions. This point allow us to speculate that the high-annealing temperature drives the conversion of the insulating behavior of ZnS surface into a semiconducting structure. All these aspects will be carefully examined next.

Discussion

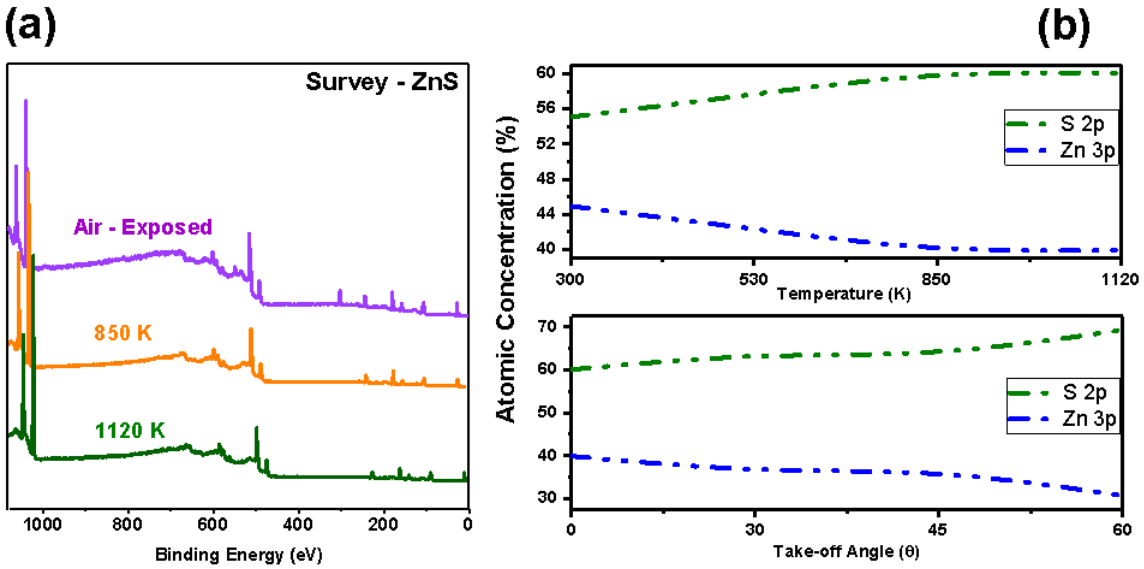

Figure 4.7: Impacts of high surface treatment on XPS experiments. *(a) Evolution of the binding energies positions as function of the annealing temperature; (b) Evolution of the atomic concentration as function of both annealing temperature (top) and take-off angle (bottom).*

The degree of influence of high surface treatment condition on ZnS(001) single crystal are discussed from XPS analysis depicted in Figure 4.7. Figure 4.7-(a) presents three differents survey spectra. Initially, in absence of surface treatment (purple line spectrum), the main peaks lie at 1035.67, 512.87, and 157.11 eV, associated to Zn 2p, Zn LMM, and S 2p, respectively. These binding energies are higher than their typical values and even than those discussed in the last section, reinforcing the weakness of the previous surface treatment. In the sequence, an appreciable shift reduction was observed: Zn 2p, Zn LMM, and S 2p components

arisen at 1031.8, 510 (979.54), and 173 eV, correspondingly, then configuring a shift of 10 eV.

Although the slight increase in the energy shift, this new scenario seems to be much stable than the previous one. Charging increasing during XPS acquisition was not observed, and we noted a good refinement in the spots resolution in LEED experiments (but still insufficient to realize some geometrical modifications) . In view of these promising results, we increased the annealing temperature up to 1120 K (green line spectrum in Figure 4.7-(a)). In this scenario, the charging was almost[2] removed, as indicated by the Zn 2p and S 2p binding energies and Zn LMM kinetic energy: 1021.8, 161.8 and 988.07 eV, respectively.

All of them were obtained without ion gun support. Recalling the second point highlighted in the last section, one can address this finding to the formation of a cation-defectiveness structure, which means a sulfur-rich ZnS surface in this case. More details about this issue is derived by the atomic concentration. In this step the contribution of the S 2p and Zn 3p orbitals was analyzed as a function of the annealing temperature [3]. As shown in Figure 4.7-(b) (top graphic), S 2p concentrations increased 5%, confirming the assumption of a sulfur-richer ZnS surface, derived by the preparation condition. As earlier speculated, the removal of zinc atoms might favors ZnS atoms to undergo geometrical modifications, which means cation and anions moving inward and outward to the surface (according to theoretical calculations previously reported [23])

This fact implies a higher prevalence of sulfur atoms at the topmost layers of the ZnS surface. In this context, novel XPS survey spectra were acquired by varying the take-off angle and then another quantification of the atomic concentration as a function of such a parameter was carried out[4]. The result shown in Figure 4.7-(b) (bottom graphic) is in good agreement with the expectation of a higher prevalence of sulfur atoms at the topmost layers, in view of the increase of 10% from normal to angled emission .

We now turn our attention to the high resolution spectra showed in Figure 4.8(a) and (b), comparing the intermediate (at 850 K) and the highest surface treatment (at 1120 K), respectively. Starting from Zn 2p components (left spectra in both panel) it can been noted in all scenarios the spin-orbit splitting of 23 eV. In addition, the FWHM measurements depicted in each spectra are in good agreement with previous results on sulfide systems [80] and those reported with flood

[2]There is a small shift of 0.6 eV compared to the spectra acquired with flood gun assistance

[3]One recording the discussion in chapter 3: The photoelectrons of such components emerges from the same depth

[4]One recording the discussion in chapter 3: Angled acquisition decrease the electron-mean free path deriving more information from the top surface layers

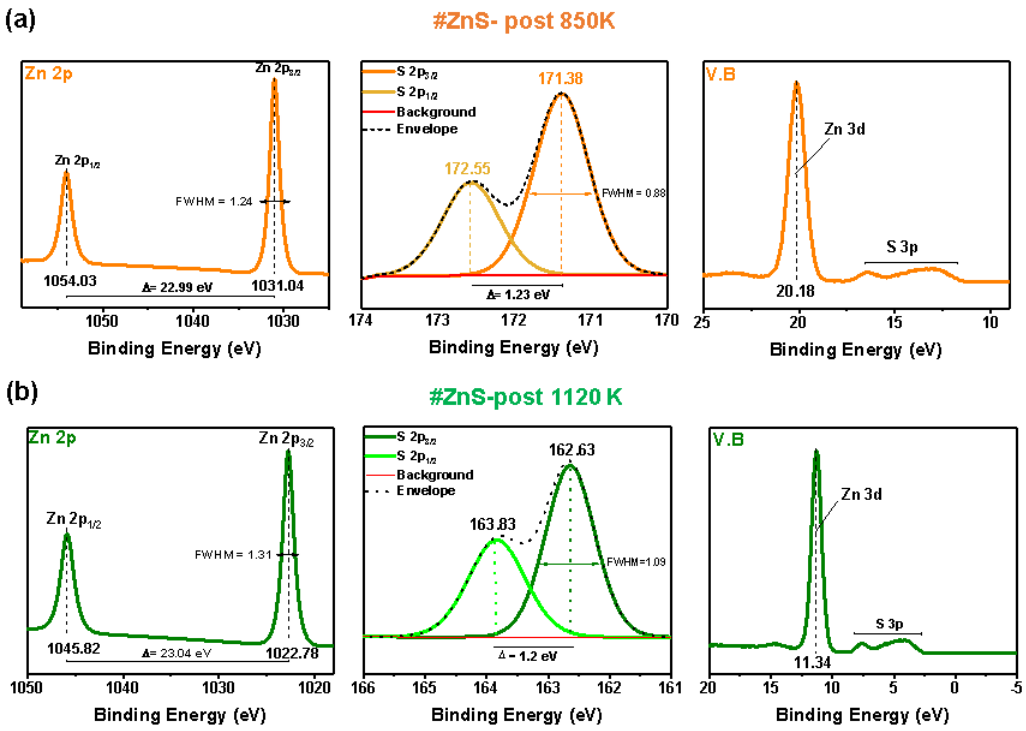

Figure 4.8: High resolution spectra of the high treated sample at *(a) 850 K ; (b) 1120 K. All the spectra were carried out at room temperature*

assistance discussed in the last section. Notable differences were restricted to the correction of binding energy positions only. Similar findings holds for S 2p component (middle spectra) and valence band region (right spectra).The spin-orbit split of 1.6 eV between S $2p_{3/2}$ and S $2p_{1/2}$ is consistent with correlated investigations. Moreover, it was not observed different contributions apart from S^{2-} and Zn^{2-} state. The contribution of Zn 3d in the valence band and the final contribution from S 3p were also obtained without spurious contribution, in good agreement with the density of states calculations. These findings allow us to speculate that the modifications driven by the annealing temperature have an intrinsic characteristic, which means the chemical status of the system is preserved. Hence one can rationalize the high surface treatment favor the formation of a sulfur-richer surface only. Further, such dominance is pronounced at the topmost layers of the ZnS Surface. This fact can be addressed to the segregation mentioned in the last section, reflected by the slight broadening in the FWHM measurements of the S 2p components in the S-richer ZnS surface scenario.

Fundamental results indicating an enhancement in the ZnS surface conductivity are the LEED patterns shown in Figure 4.9 (a)-(b). It can be noted (in both figures) a square unit cell with a lattice parameter of 3.82 Å(see chapter 3 to recall the calculation procedure), in appreciable agreement with theoretical calculations reported in the literature and the arrangement mentioned in chapter 1.

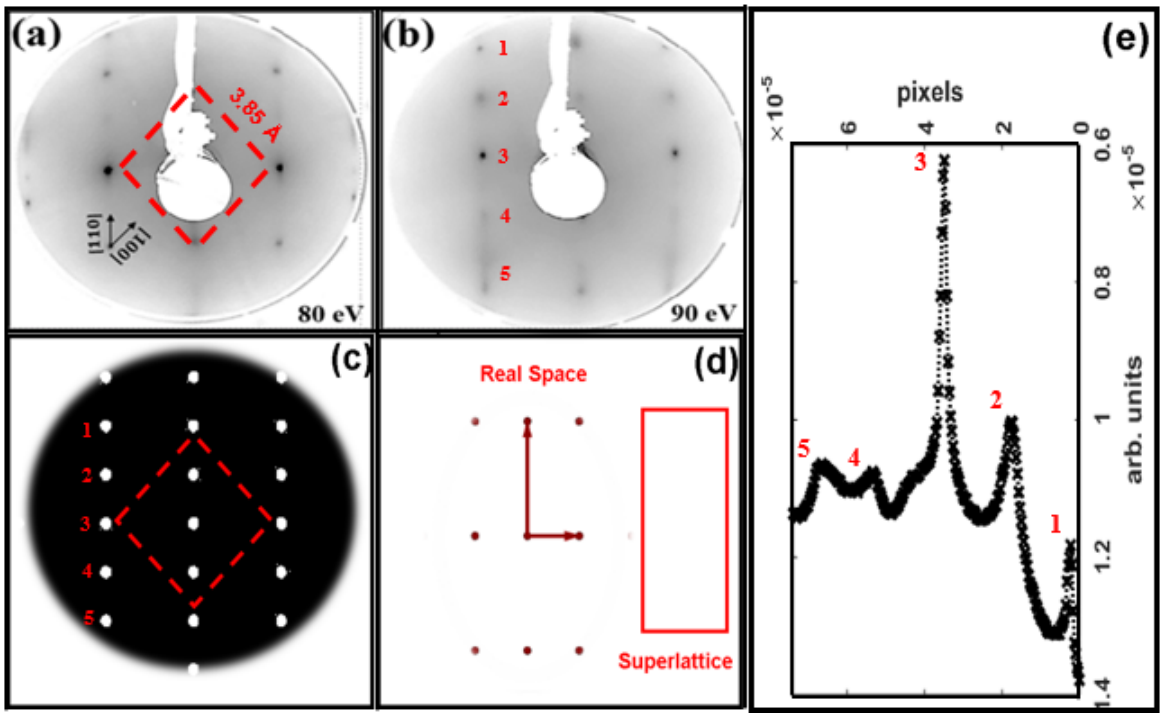

Figure 4.9: LEED Pattern of the ZnS structure. *Experimental results achieved with (a) 88 eV and (b) 80 eV of electron energy. Simulated (c) reciprocal space (d) real space of the (1 x 2) reconstructed surface.(e) Line profile to emphasize the five Brag spots*

Interesting to be noted is the higher directionality assigned by the alternate row along [110] direction. This fact reflects the covalent nature of the ZnS bonds, as discussed in chapter 2. The particular arrangement revealed experimentally agree very well with the (1 x 2) structure predicted from LEEDpat simulation [67], as depicted in Figure 4.9- (c) and (d). One can note in Figure 4.9 (b) five Bragg spots in a row, identically as the simulated structure depicted in Figure 4.9 (c). In view of the poor resolution of some spots, a line profile plot was performed from Figure 4.9 (b), as showed in Figure 4.9 (e), thereby confirming the presence of five diffraction maxima in the row. From this result a translation symmetry breaking along [110] direction is indicated. This finding is corroborative to the cation-vacancy driven surface reconstruction hypothesis.

This kind of reconstruction is characterized by a missing row of atoms. It was reported in the literature for other single crystals, as discussed by *Kellog* in the investigation upon Pt single crystal. The author demonstrated that temperature can drives this geometrical modifications, especially on FCC structures [81]. In view of the present results, we can speculate that the missing row in the ZnS are provided by the removal of zinc species, due to the high-surface treatment. Thus geometrical reconstruction is linked to preparation conditions too. Although the spots do not lie sharp enough as expected in LEED experiments (in view of the

still insulating aspect, certainly), these results provide appreciable evidence of the conversion of the ZnS surface into a semiconducting structure.

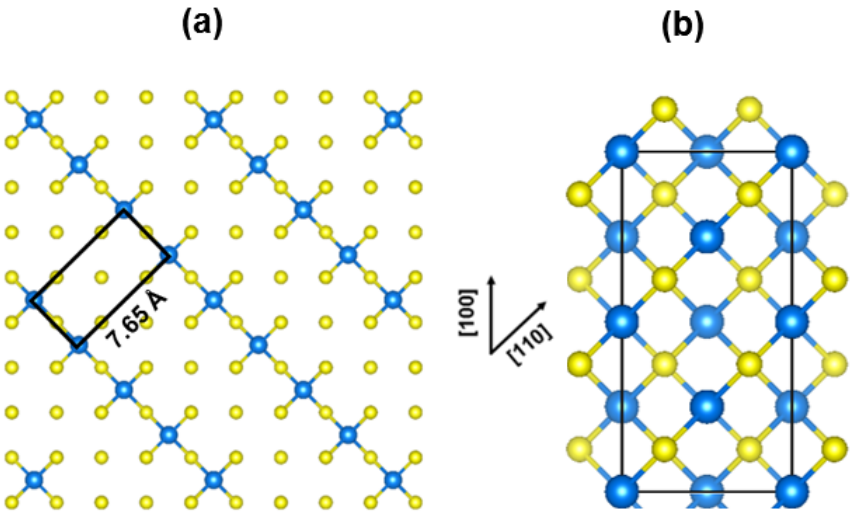

Figure 4.10: Empirical proposed model. *(a) We assumed a* (1×2) *surface reconstruction along [110] direction; (b) and consider a more simplified* 1×2 *structure without Zn vacancies. The hydrogen atoms are not shown for arbitrary choice.*

Based on the experimental results we proposed an empirical model consisting of a (1 x 2) reconstructed unit cell, derived by alternate missing row of Zn atoms, as depicted in Figure 4.10-(a). In this context, we expected an ideal scenario of surface conductivity, which can be indirectly derived by first-principles calculation . However, DFT calculations on defectiveness surfaces are very expensive in terms of computational costs and are very complex to deal in terms of convergence (at least in the particular case of ZnS surface, as will be briefly discussed in Appendix II). In view of this, we investigated a similar 1×2 structure [5]. Such a model is consisted of a 1×2 slab as illustrated in Figure 4.10-(b), whereby we defined new basis vectors such that along $\hat{\mathbf{y}}$ the slab thickness is duplicated[6]. In this structure, one can note a peculiar behavior on the top layers by comparing the initial system with the optimized slab (derived by several self-consistent calculations keeping the volume cell and varying the positions of the ions) depicted in Figure 4.11-(a) and Figure 4.11 -(b), respectively.

For instance,the typical distance between the internal sulfur atom (denoted by S_{int}) from the top sulfur atoms (denoted by S_{top}) is 8.59 Å. However, this value has raised to 8.80 Åafter the optimization. Since the internal S atom was kept fixed, this increase on the distance must be related with outwards dislocations

[5] Henceforth simulated structures will be mentioned without parenthesis

[6] This structure is obtained not only duplicating the 1×1 slab. In addition, in the $\hat{z}$ direction there is a vacuum of 15 Å, as discussed in chapter 3

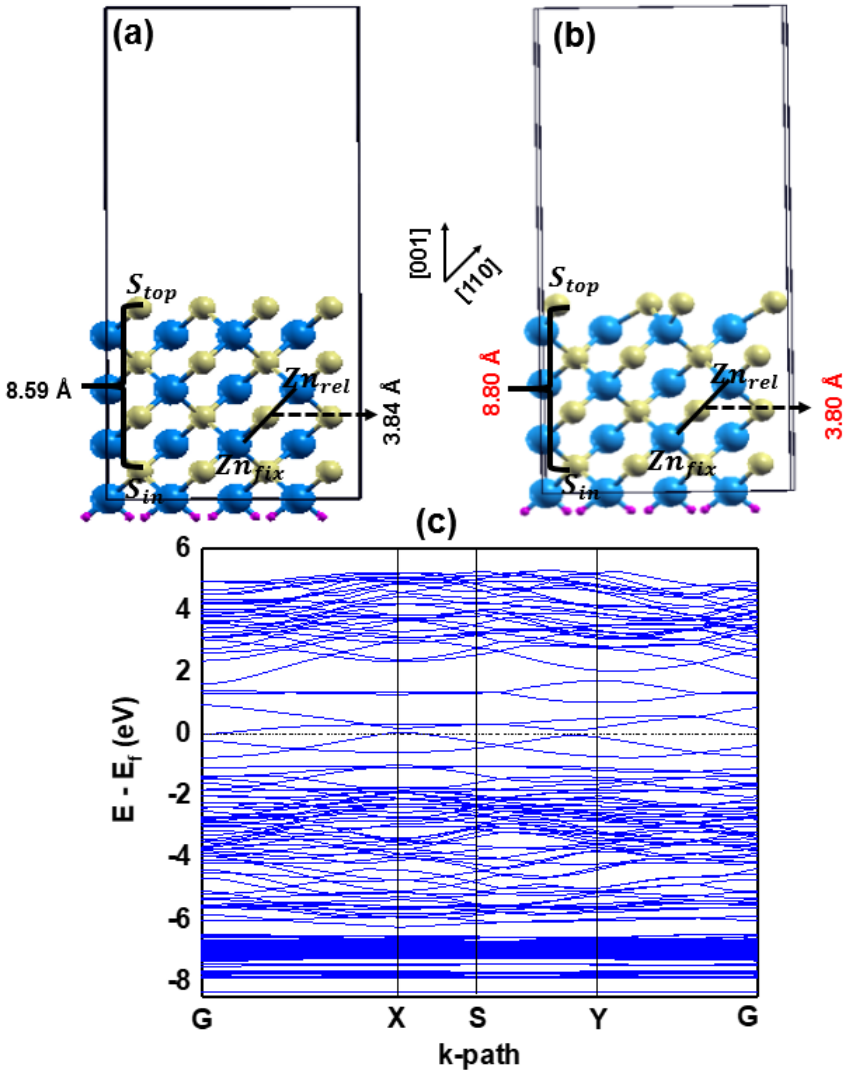

Figure 4.11: Electronic structure of the 1×2 ***ZnS surface.*** *Initial (a) and optimized (b) atomic positions ; (c) Band structure of the system.*

to the surface of the top S atoms. Conversely, the distance between the relaxed Zn atom (labeled Zn_{rel}) to the fixed Zn specie (labeled as Zn_{fix}) decreased from 3.84 Åin the initial structure to 3.80 ÅÅin the optimized configuration. Then we can rationalize that the top zinc atoms tends to move inwards to the ZnS surface. Such displacements, as mentioned in this thesis, are indeed expected in the case of a ZnS reconstructed surface, which lead us to speculate that the existence of a (1×2) ZnS surface is conditioned to a surface reconstruction, which in this work is assumed to be driven by the removal of Zn species. These peculiar modifications in the atomic positions were not observed in the case of a 1 x 1 structure. Moreover, in view of the opposite dislocation of Zn and S species one can speculate that such a crystallographic arrangement give rise to an apparent S excess at the top layers of the ZnS surface, in good agreement with XPS results. This anionic excess at the ZnS surface are translated into several states with a

semi metallic-like character provided by S 3p states that lying in the forbidden zone, as depicted in Figure 4.11-(c).

Based on these findings, the (1×2) slab can be addressed to the ideal scenario in which the structure has an excess of sulfur atoms at the topmost layers and apparently a more semiconducting nature, translated into several surface states populating the forbidden zone. Therefore, we can conclude that besides confirming the experimental findings regarded to sulfur dominancy in a reconstructed ZnS system, such calculations are another indirect signature of the conversion of the insulating ZnS surface into a semiconducting system.

Conclusion

In this section, we evaluated the degree of influence of high-temperature surface treatment conditions. We observed that this scenario favors the removal of Zinc atoms, and can be understood as a cation-doping mechanism. The prevalence of Sulfur atoms over zinc species is pretty appreciable at the topmost layers of the ZnS surface, as revealed by performing the atomic concentration as function of the take-off angle. Despite this sulfur-richer surface scenario, there is no modification on the chemical status of the structure, since the typical components and main aspects were not altering.

On the other hand, modifications on the geometrical arrangement were noted from LEED experiments, which indicates the formation of a (1 x 2) reconstructed surface characterized by the missing row of atoms. In view of the mentioned Sulfur excess, we speculate the missing atoms are derived by the removal of Zinc elements due to the high surface treatment conditions. These experimental findings suggest a cation defectiveness surface, which seem to be more semiconducting than the pristine structure discussed in the last section. The speculation of an enhancement on the ZnS surface conductivity was indirectly endorsed by first-principles calculations, which evaluated the electronic structure of the ZnS (001)-1x2 surface slab. The theoretical findings reveal several surface states in the forbidden zone with a semi-metallic character. Hence based in this finding we can conclude that :

1. High-temperature surface treatment implies the removal of Zn species;
2. The removal of Zn species lead the formation of a (1 x 2) reconstructed Surface
3. The reconstructed surface is more semiconducting.

Chapter 5

Conclusions and Future Work

In this work, the ZnS (001) Surface was investigated by XPS and LEED experiments. In addition, some DFT calculations complemented our experimental findings. XPS experiments revealed that in absence of surface treatment, the ZnS components arise at higher binding energy due to the charging effect. This scenario is dramatically modified by increasing the annealing temperature. Post such an improvement on the surface preparation, the XPS peaks arisen at the correct binding energy position even without ion gun assistance. It is assumed that high-temperature preparation conditions drive the formation of native cation-defects at the ZnS surface since the analysis of atomic concentration at differents conditions revealed an increase on the sulfur concentration over zinc species as a function of the annealing temperature. By acquiring the XPS spectra at different take-off angle, the predominance of sulfur species over zinc was emphasized. This fact does not entail chemical modifications since the H.R spectras revealed that the aspects of zinc and sulfur bonding in Zn^{2+} S^{2-} configuration is preserving.

It is well-known (from the theoretical point of view) that point defects at ZnS surface favors the geometrical reconstruction in this system, however this fact has not not been reported experimentally yet . In this work, after the distinguished preparation condition (high annealing temperature), this hypothesis was confirmed from LEED experiments, revealing a symmetry breaking along [110] direction consisting of a missing row of atoms. In view of the XPS experiments that shown an excess of S atoms, we speculated that the missing atoms has a cationic nature. In addition, the diffraction pattern is consistent with a (1 x 2) surface reconstruction. Thus we rationalized that the surface treatment drives the formation of a (1 x 2) reconstructed and cation defectiveness surface. Furthermore, we speculated that the reconstructed ZnS surface is the ideal scenario concerning to surface conductivity. This hypothesis was supported by DFT calculations, which revealed semi-metallic states almost filling the entire forbidden zone. These

states are provided by S 3p states, reinforcing the dominancy of Sulfur atoms at the topmost later of the reconstructed ZnS system, as indicated by experimental results.

Despite the consistent results reported in this thesis, there are still unsolved questions that must be emphasized in next investigations. For instance, we have speculated about the formation of cation defects on the ZnS surface. However, it is possible to obtain cation vacancy at a bulk level too. In this regard, one may argue about the degree of influence on electronic and optical properties. On the first topic, we have started the analysis (See Appendix II) and noted that in the experimental limit of doping, defectiveness ZnS bulk is independent of the amount of point defects. On the later topic, our collaborators have carried out Raman Spectroscopy experiments on the treated sample and noted that this scenario gives rise to a luminescence component. Hence one can speculate that vacancies at bulk level play an interesting role on the optical properties of this system. This finding must be carefully examined together with first-principles calculations.

From the theoretical viewpoint, it is convenient to explore the formation of defects on the surface. Although this task has a large computational demand, our initial calculations (see appendix II) suggests interesting aspects such as the peculiar format provided by the new states in the forbidden zone. Further, we must to investigate the charge states of these defects, which does not seem an immediate task. Moreover, we must quantify the modifications on the gap either in the defectiveness slab as in the reconstructed system. Once in this dissertation we were interested in indirect signatures to support some speculations regarding to the conversion of the ZnS surface into a more conductivity system, this point was neglected. However, for a complete understanding on the electronic structure of the mentioned systems, it is worth expend more time improving the calculations with assistance of hybrids functional, for instance.

Closing, a crucial aspect that must be investigated is the extension of the results presented in this work. Apparently, XS-like systems (being X a transition metal) are insulating and generally unstable. Then we may argue if the formation of a defectiveness structure might be the ideal route towards converting these structures into a semiconducting systems, which might facilitates the application of some surface science experimental tools, such as XPS and LEED, and hence increase the knowledge regarding to surface peculiarities of these structures. We cannot precise the degree of influence of such a mechanism on other sulfide structures, at this moment. However, given the results exposed in this work, it seems to be a very promising strategy.

A1. Brief comments on DFT calculations

DFT is one of the most efficient methods for electronic structure calculations in condensed matter physics. From this formalism, one can convert the N-electrons problem into a set fo N-single-particle problem. This purpose is familiar to the Hartree-Fock theory. However, in the later case, the heart of the model is the wave function ψ, whereas in the DFT formalism the total electronic density $\rho(r)$ is the fundamental parameter. Such a simplification was demonstrated by *Hohenberg* and *Kohn* in 1964 [82]. These authors established two theorems that are the base of the DFT and state that:

Theorem 1. *The external potential* $v(\mathbf{r})$ *is a unique functional of the electronic density* $\rho(\mathbf{r})$*.*

Theorem 2. *The ground state energy* $E_0[\rho]$ *is minimum for the exact electronic density.*

Both theorems can be easily proofed, as demonstrated in [83], however, this step is not the focus in this section. A crucial result on DFT was developed by *Kohn* and *Sham*, which derived the *Kohn-Shan equations*. The mechanism to achieve the DFT propose (convert the multielectronic problem into N single particle problems) was obtained from these equations. It can be derived as follow. Considering the energy functional

$$E[\rho] = \int v(\mathbf{r})\rho(\mathbf{r})d^3r + \frac{1}{2}\int\int \frac{\rho(\mathbf{r})\rho(\mathbf{r}')}{|\mathbf{r}-\mathbf{r}'|}d^3r d^3r' + T_0[\rho] + \int \rho(\mathbf{r})E_{xc}(\rho(\mathbf{r}))d^3r \ . \quad \text{(A.1)}$$

Fixing the electronic charge, i.e

$$\int \rho(\mathbf{r})d^3r = N, \quad \text{(A.2)}$$

and applying the extreme condition on (A.1) one obtain [83]:

$$\int \delta\rho(\mathbf{r}) \left\{ \frac{\delta T_0}{\delta\rho} + v(\mathbf{r} + \int \frac{\rho(\mathbf{r}'}{|\mathbf{r}-\mathbf{r}'|} d^3r' + v_{xc} - \mu \right\} d^3r = 0. \tag{A.3}$$

In (A.3), v_{xc} is the exchange-correlation potential defined as [83]:

$$v_{xc}[\rho] = \frac{\delta E_{xc}}{\delta\rho} \tag{A.4}$$

The kinetic energy can be expressed as:

$$T_0[\rho] = -\frac{1}{2} \sum_i \int \psi_i^* \nabla^2 \psi_i d^3r. \tag{A.5}$$

Combining with the auxiliary charge density

$$\rho(\mathbf{r}) = \sum_i^N |\psi(\mathbf{r})|^2, \tag{A.6}$$

we can solve (A.3) by solving the single particle Schrodinger equation given by [83]:

$$\left(-\frac{1}{2}\nabla^2 + v^{KS}[\rho] \right) \psi_i(\mathbf{r}) = \epsilon_i \psi_i(\mathbf{r}). \tag{A.7}$$

where

$$v^{KS} = v(\mathbf{r}) + \int \frac{\rho(\mathbf{r}')}{|\mathbf{r}-\mathbf{r}'|} d^3r' + v_{xc}(\rho), \tag{A.8}$$

is the effective Kohn-Sham potential. One can note the such a potential depends on ρ. On other hand, this quantity will depends on v^{KS}. Therefore to achieve the solution, the Kohn-Sham equation (A.7) must be me solved by a self-consistent cycle [72, 83]. A schematic illustration of such a process is given by Figure A.1.

An important aspect is the a *priori* choice of the exchange-correlation functional. Such a quantity is not exact, and then we must to resorted to some of the available approximations. Two of the main approaches are the Local Density Approximation (LDA) and the Generalized Gradient Approximation (GGA). In the first model it is assumed smooth variations on $\rho(\mathbf{r})$ near to $\mathbf{r}$. In addition, it consider the exchange correlation ϵ_{xc}^h per electron of a homogeneous electrons gas with density ρ continuous in all space. Hence, it can be denoted as:

$$E_{xc}[\rho] = \int \rho(\mathbf{r}) e_{xc}^h(\rho(\mathbf{r})) d^3r. \tag{A.9}$$

However, in the case of non-uniformity on the electronic density, this approximation is not appropriated To avoid this problem, GGA model takes into account the gradient of the charge density instead the electronic density only, as discussed

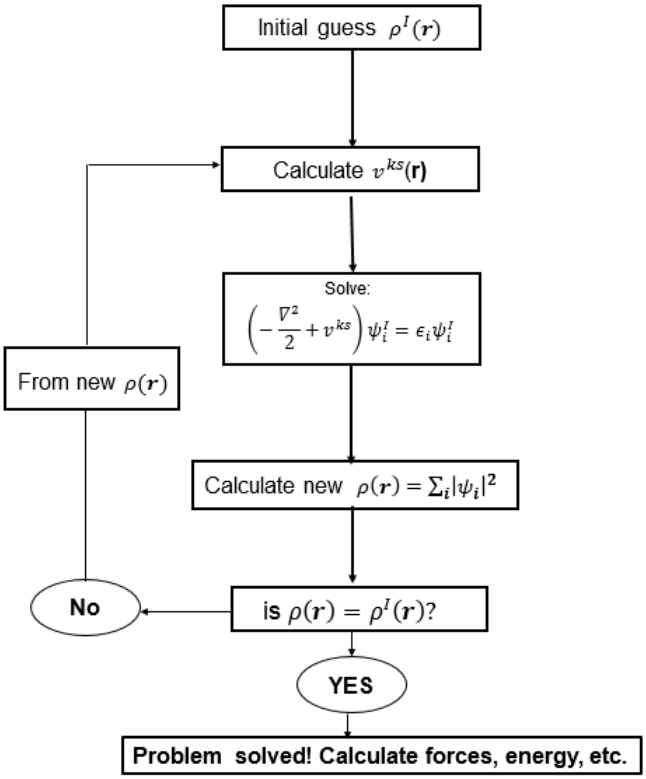

Figure A.1: The SCF cycle.

by *Perdew, Burke, and Erzenhof* that derives the most used model for the GGA approach. Commonly, it can be denoted as follow [83]:

$$E_{xc}^{GGA}[\rho] = \int f(\rho(\mathbf{r}), \nabla\rho(\mathbf{r}))d^3r. \tag{A.10}$$

Currently, there are novel methodologies that enhance the description of the exchange-correlation terms, and then improve some calculations such as the energy gap, which tends to be underestimated by using the PBE description. Nonetheless, the reader can found a complete discussion of such issues in [84] and [85], for instance. Here we restricted the discussion to the general aspects of the DFT. Now we turn our attention to describe the main parameters used in the calculations.

Elementary calculations on ZnS

A fundamental aspect of the DFT calculations is the convergence test. This is the initial step forward to scientific calculations. In this stage we must to understand and recover some fundamental properties of the system, such as density and lattice parameter, in terms of the ideal cutoff energy and k-points sampling. In this work we take as reference a comparative investigation among the ZnS structures: ZB, WZ and Rock Salt (rs). For this purpose, we simulate the most simple arrangement of ZnS consisting of two atoms per unit cell. Initially, we compared the total energy of ZB and WZ structures as function of the cutoff energy,and noted that the total energy minimum was achieved for a cutoff energy of $44Ry$. In addition, by comparing the total energy of both structures we observed that indeed the ZB structure is most stable than the WZ one, as the first has -310.14 Ry of the total energy minimum whereas the last structure demands -309.99 Ry, thereby configuring a energy difference at about 14.28 eV.

K-points grid	Volume (Å^3)	Energy (eV)	Density (g/cm^3)
10 x 10 x 10 |14 x 14 x 14	40.27 |33.22	0.000 |0.639	4.03 |4.87
8 x 8 x 8 |12 x 12 x 12	40.27 |33.22	0.000 |0.639	4.03 |4.87
6 x 6 x 6 |10 x 10 x 10	40.28 |33.22	0.000 |0.639	4.02 |4.87

Table A.1: *Preliminary results on the ZnS structures: ZB / rs. The cutoff energy was kept constant.*

Sequentially, based on the investigation of [39] we compared the properties of the ZB and rs structure [1]. Regarded to the methodology, it can be described as follow: Initially, the positions of the ions are kept constant and the volume cell will relax. In the final configuration, we will evaluate the lattice parameter of each system. In this stage we obtained 5.44 Åfor the ZB structure and 5.10 Åfor the rs, in good agreement with the literature results, which reveals 5.41 and 5.07 Åfor ZB and rs, respectively. Sequentially, by varying the k-points grid in the reciprocal space and maintaining the cutoff energy for wave function constant (at 44 Ry) we compared the energy difference, volume, and density of each system. In this part, the total energy of the ZB structure will be assumed as null, and total energy of the rs system with respect to the ZB will corresponds to the energy difference between both configurations, that is 0.639 eV according to [39]. In Table A.1 we summarize all the calculations

From this results we assumed the best k-points grid as 6 x 6 x 6. Sequentially,

[1] The rs structure was neglected during the discussion in this thesis, because there is no experimental evidence of its stability, although some theoretical works emphasize its properties.

fixing such a grid of points, we evaluated the same quantities, but now varying the cutoff energy. In this scenario, we noted that 38 Ry is a suitable choice for the wave functions, since in this configuration there are no substantial changes on the properties of the system, as depicted in A.2

E_{cutt} (Ry)	Volume (Å^3)	Energy (eV)	Density (g/cm^3)
44	40.12 | 33.19	0.000 |0.639	4.03 |4.87
42	40.26 | 33.21	0.000 |0.639	4.02 |4.87
40	40.25 | 33.21	0.000 |0.639	4.02 |4.87
38	39.94 | 33.22	0.000 |0.639	4.02 |4.87

Table A.2: *Preliminary results on the ZnS structures: ZB \| rs. The k-points grid was kept constant.*

B. Zn-vacancy on ZnS: Preliminary DFT calculations

In this section, we report some initial calculations on a defectiveness slab. At this moment, we discussed the degree of influence of cation defects on the ZnS surface only. However, it might play a role at a bulk level too. As mentioned in chapter 5, initial experiments with Raman spectroscopy suggest the removal of Zn species at a bulk level perhaps enhances the optical properties of the ZnS. In view of this, we duplicate the fundamental slab along $\hat{\mathbf{x}}$ and $\hat{\mathbf{y}}$ direction in order to construct a slab with 64 atoms. Sequentially, we removed one Zn atom and evaluate the electronic structure of such a system with 1.56 percent of impurities. In addition, we increased the impurities percentage by simulating a similar slab, but with two-absent zinc atoms. The band structure of each configuration is depicted in Figure B.1-(a) and Figure B.1-(b), respectively.

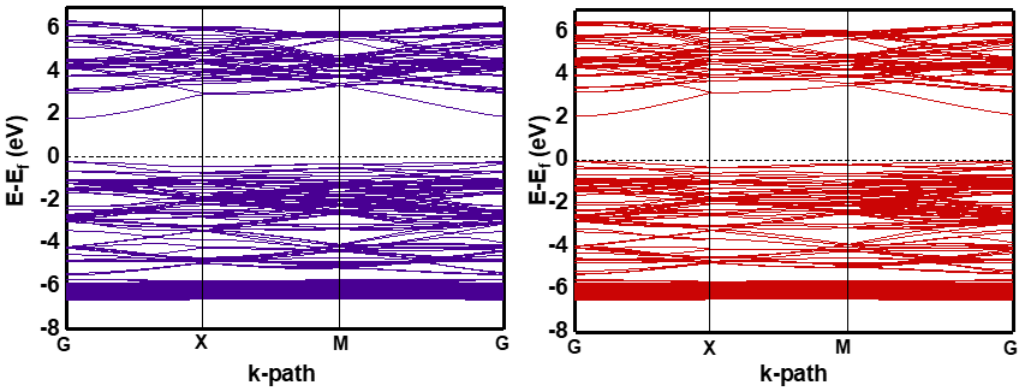

Figure B.1: Band structure of defectiveness ZnS bulk. *(a) One zinc atom removed ; (b) two zinc atoms removed. All calculations were carried with spin-polarization.*

Curiously, both calculations do not reveal states on the forbidden zone. The modification in this cation-defectiveness structure is the Fermi level position, which in the first case (1 Zn atom absent) lies near (but not at) the valence band top (as shown in Figure B.1 -(a)), and tends to be coincident with the valence band maximum in the higher cation-defectiveness scenario (as shown in

Figure B.1 -(b)). This result allows to speculate the removal of Zn atoms at bulk level does not drives the formation of semi-metallic states in the forbidden zone, but lead the formation of a degenerated structure. In all scenarios, the valence band maximum and the conduction band minimum are separated by 2.02 eV, as in the case of pristine bulk structure. Therefore we speculate that, at least in the experimental limit of doping ($< 7\%$), the bulk ZnS seems to hold its insulating characteristic. These results might explain the impossibility to perform STM experiments: Although the preparation conditions at high annealing temperature drive the conversion of the insulating ZnS surface into a semiconducting structure, this behavior is restricted to the first layers only. At the bulk level, the system still behaves as insulating, and then no tunneling current can be detected. Further to this insulating feature, the non-magnetic properties of such a system seem to be strong. In all calculations, we considered spin polarization along $\hat{\mathbf{z}}$ direction. In this context, we observed that such calculations have been converged, nevertheless the total and local magnetization are null.

Concluding, we performed some calculations for defects in the ZnS Surface. Similar to bulk structure, we duplicated the primitive slab along $\hat{\mathbf{x}}$ and $\hat{\mathbf{y}}$ directions, then obtaining a 2 x 2 x 1 supercell with 80 atoms, whereby 64 are from ZnS and the remaining contributions come from hydrogen atoms, as mentioned in chapter 3. Hence two zinc atoms were removed from the topmost-layers, therefore we constructed a slab with 6.25% of impurity. The band structure of such a system is depicted in Figure B.2.

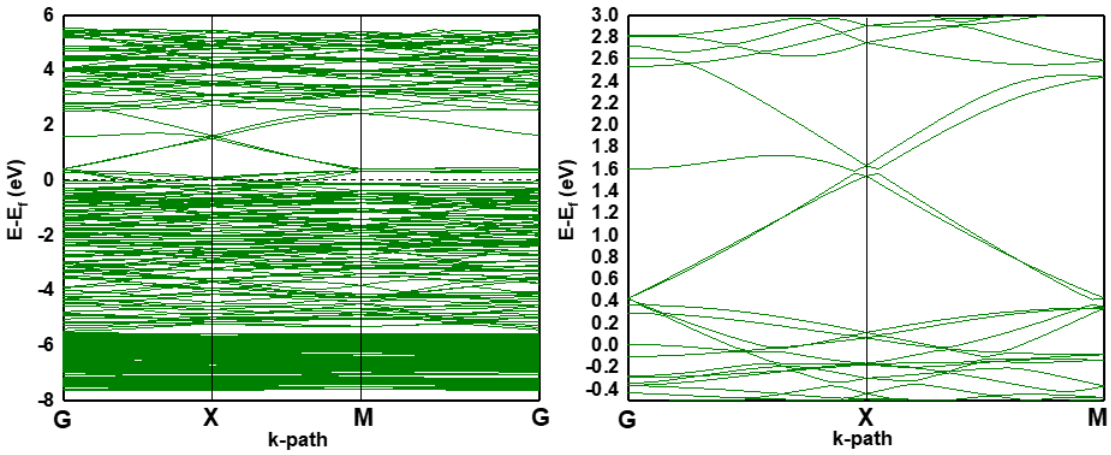

Figure B.2: band structure of defectiveness ZnS Surface. *(a) The total band structure and (b) a small portion of the band structure containing states in the forbidden zone.*

It is worth noting the semi-metallic like states rising in the forbidden zone. This result indicates that indeed the formation of cation defects plays a crucial role on the electronic structure of the ZnS system. Further interesting is the aspect of such states, depicted in Figure B.2-(b). They originate a high-dispersivity structure, that remember a Dirac cone (but of course it is just a similarity). The absence of a gap is addressed to the limitations on GGG-PBE, which reflects the need to improve the description of the exchange-correlation energy. Future enhancements in the calculations can give more evidence to unveil the peculiarities of this cation-defectiveness ZnS surface. For now, these partial results reflect that we still have several works to do in this system .

Bibliography

[1] D. A. Neamen, Semiconductor physics and devices: basic principles, New York, NY: McGraw-Hill,, 2012. 1.1

[2] S. P. Jiang, A review of wet impregnationan alternative method for the fabrication of high performance and nano-structured electrodes of solid oxide fuel cells, Materials Science & Engineering A 418 (1-2) (2006) 199–210. doi:10.1016/j.msea.2005.11.052. 1.1

[3] R. Woods-Robinson, Y. Han, H. Zhang, T. Ablekim, I. Khan, K. A. Persson, A. Zakutayev, Wide band gap chalcogenide semiconductors, Chemical reviews 120 (9) (2020) 4007–4055. 1.1, 2.1

[4] D. Yadav, D. Singh, Static and dynamical properties of ii–vi and iii–v group binary solids, Physica Scripta 85 (1) (2011) 015701. doi:10.1088/0031-8949/85/01/015701. 1.1

[5] O. Brafman, S. Mitra, Raman effect in wurtzite-and zinc-blende-type zns single crystals, Physical Review 171 (3) (1968) 931. doi:10.1103/PhysRev.171.931. 1.1

[6] F. d. A. La Porta, A. Nogueira, L. Gracia, W. Pereira, G. Botelho, T. A. Mulinari, J. Andrés, E. Longo, An experimental and theoretical investigation on the optical and photocatalytic properties of zns nanoparticles, Journal of Physics and Chemistry of Solids 103 (2017) 179–189. doi:10.1016/j.jpcs.2016.12.025. 1.1, 4.1, 4.1

[7] A. T. Salih, A. A. Najim, M. A. Muhi, K. R. Gbashi, Single-material multilayer zns as anti-reflective coating for solar cell applications, Optics Communications 388 (2017) 84–89. doi:10.1016/j.optcom.2016.12.035. 1.1

[8] K. Momma, F. Izumi, Vesta: a three-dimensional visualization system for electronic and structural analysis, Journal of Applied crystallography 41 (3) (2008) 653–658. doi:10.1107/S0021889808012016. 1.1

[9] K. S. Novoselov, A. K. Geim, S. V. Morozov, D. Jiang, Y. Zhang, S. V. Dubonos, I. V. Grigorieva, A. A. Firsov, Electric field effect in atomically thin carbon films, science 306 (5696) (2004) 666–669. doi:10.1126/science.1102896. 1.1

[10] Y. Ma, L. Qi, J. Ma, H. Cheng, Facile synthesis of hollow zns nanospheres in block copolymer solutions, Langmuir 19 (9) (2003) 4040–4042. doi:10.1021/la026997w. 1.1

[11] Z.-G. Chen, L. Cheng, H.-Y. Xu, J.-Z. Liu, J. Zou, T. Sekiguchi, G. Q. Lu, H.-M. Cheng, Zns branched architectures as optoelectronic devices and field emitters, Advanced Materials 22 (21) (2010) 2376–2380. doi:10.1002/adma.200903643. 1.1

[12] X. Wang, Z. Xie, H. Huang, Z. Liu, D. Chen, G. Shen, Gas sensors, thermistor and photodetector based on zns nanowires, Journal of Materials Chemistry 22 (14) (2012) 6845–6850. doi:10.1039/C2JM16523F. 1.1

[13] J. Cheng, D. Fan, H. Wang, B. Liu, Y. Zhang, H. Yan, Chemical bath deposition of crystalline zns thin films, Semiconductor science and technology 18 (7) (2003) 676. doi:10.1088/0268-1242/18/7/313. 1.1

[14] G. A. Somorjai, J. Y. Park, Concepts, instruments, and model systems that enabled the rapid evolution of surface science, Surface Science 603 (10-12) (2009) 1293–1300. doi:10.1016/j.susc.2008.08.030. 1.1, 3.2.1

[15] F. Pesty, P. Garoche, Low-energy electron beam on an insulator surface: Impact of the charging process on the diffraction by mica muscovite, Surface science 580 (1-3) (2005) 153–162. doi:10.1016/j.susc.2005.02.018. 1.1

[16] S. Adachi, Wiley series in materials for electronic and optoelectronic applications, Capper, P (2005). 2.1, 2.1, 2.2, 2.4

[17] M. Grundmann, Physics of semiconductors, Vol. 11, Springer, 2010. 2.1, 1

[18] A. Nilsson, B. Eriksson, N. Mårtensson, J. Andersen, J. Onsgaard, Core-level binding-energy shifts during metal adsorption and compound formation: Yb/ni (100), Physical Review B 38 (15) (1988) 10357. doi:10.1103/PhysRevB.38.10357. 2.1

[19] M. D. McCluskey, E. E. Haller, Dopants and defects in semiconductors, CRC press, 2018. 2.1, 2.2

[20] M. A. Nielsen, I. Chuang, Quantum computation and quantum information (2002). 2.1, 3.1.1

[21] M. Cardona, Y. Y. Peter, Fundamentals of semiconductors, Springer, 2005. 2.2, 3.1.1

[22] F. Bechstedt, Principles of surface physics, Springer Science & Business Media, 2012. 2.2, 2.4, 2.6, 2, 2.4, 2.4, 2.4, 2.4, 2.4, 3.2.2

[23] K. Wright, G. Watson, S. Parker, D. Vaughan, Simulation of the structure and stability of sphalerite (zns) surfaces, American Mineralogist 83 (1) (1998) 141–146. doi:10.2138/am-1998-1-214. 2.2, 2.5, 4.2

[24] C. Noguera, Polar oxide surfaces, Journal of Physics: Condensed Matter 12 (31) (2000) R367. doi:10.1088/0953-8984/12/31/201. 2.3

[25] P. Tasker, The stability of ionic crystal surfaces, Journal of Physics C: Solid State Physics 12 (22) (1979) 4977. doi:10.1088/0022-3719/12/22/036. 2.3, 2.4, 2.3

[26] P. Ebert, Nano-scale properties of defects in compound semiconductor surfaces, Surface science reports 33 (4-8) (1999) 121–303. doi:10.1016/S0167-5729(98)00011-9. 2.3

[27] M.-C. Desjonqueres, D. Spanjaard, Concepts in Surface Physics: 2eme édition, Vol. 30, Springer Science & Business Media, 1996. 2.4, 2.4

[28] P. Bennett, M. Webb, The si (111) 7 × 7 to 1 × 1 transition, Surface Science 104 (1) (1981) 74–104. doi:10.1016/0039-6028(81)90125-4. 2.4

[29] W. Göpel, J. Anderson, D. Frankel, M. Jaehnig, K. Phillips, J. Schäfer, G. Rocker, Surface defects of tio2 (110): a combined xps, xaes and els study, Surface science 139 (2-3) (1984) 333–346. doi:10.1016/0039-6028(84)90054-2. 2.4

[30] X. Fang, T. Zhai, U. K. Gautam, L. Li, L. Wu, Y. Bando, D. Golberg, Zns nanostructures: from synthesis to applications, Progress in Materials Science 56 (2) (2011) 175–287. doi:10.1016/j.pmatsci.2010.10.001. 2.5

[31] J. E. Bernard, A. Zunger, Electronic structure of zns, znse, znte, and their pseudobinary alloys, Physical Review B 36 (6) (1987) 3199. doi:10.1103/PhysRevB.36.3199. 2.5

[32] M. R. Hoffmann, S. T. Martin, W. Choi, D. W. Bahnemann, Environmental applications of semiconductor photocatalysis, Chemical reviews 95 (1) (1995) 69–96. doi:10.1021/cr00033a004. 2.5

[33] F. Kurnia, J. N. Hart, Band-gap control of zinc sulfide: Towards an efficient visible-light-sensitive photocatalyst, ChemPhysChem 16 (11) (2015) 2397–2402. doi:10.1002/cphc.201500264. 2.5, 2.5

[34] H.-C. Huang, C.-L. Yang, M.-S. Wang, X.-G. Ma, Enhancement of the optical absorption of carbon group elements doped zns in the visible light range, Renewable Energy 117 (2018) 22–27. doi:10.1016/j.renene.2017.10.038. 2.5

[35] P. DAmico, A. Calzolari, A. Ruini, A. Catellani, New energy with zns: novel applications for a standard transparent compound, Scientific reports 7 (1) (2017) 1–9. doi:10.1038/s41598-017-17156-w. 2.5

[36] K. Hoang, C. Latouche, S. Jobic, Defect energy levels and persistent luminescence in cu-doped zns, Computational Materials Science 163 (2019) 63–67. doi:10.1016/j.commatsci.2019.03.016. 2.5

[37] H.-Y. Lu, S.-Y. Chu, The mechanism and characteristics of zns-based phosphor powders, Journal of crystal growth 265 (3-4) (2004) 476–481. doi:10.1016/j.jcrysgro.2004.02.011. 2.5

[38] Y. Li, J. Chen, Y. Chen, Y. Zhu, Y. Liu, Dft simulation on interaction of h2o molecules with zns and cu-activated surfaces, The Journal of Physical Chemistry C 123 (5) (2019) 3048–3057. doi:10.1021/acs.jpcc.8b12273. 2.5, 2.5

[39] C. Shahi, J. Sun, J. P. Perdew, Accurate critical pressures for structural phase transitions of group iv, iii-v, and ii-vi compounds from the scan density functional, Physical Review B 97 (9) (2018) 094111. doi:10.1103/PhysRevB.97.094111. 2.5, 5

[40] A. A. Sahraei, F. Larachi, Chemical transformation and dissociation of amino acids on metal sulfide surface: Insights from dft into the effect of surface vacancies on alanine-sphalerite system, Applied Surface Science 540 (2021) 148304. doi:10.1016/j.apsusc.2020.148304. 2.5

[41] A. A. Sahraei, F. Larachi, How do surface defects change local wettability of the hydrophilic zns surface? insights into sphalerite flotation from density

functional theory calculations, The Journal of Physical Chemistry C (2020). doi:10.1021/acs.jpcc.0c09034. 2.5

[42] H. Pang, X. Meng, P. Li, K. Chang, W. Zhou, X. Wang, X. Zhang, W. Jevasuwan, N. Fukata, D. Wang, et al., Cation vacancy-initiated co2 photoreduction over zns for efficient formate production, ACS Energy Letters 4 (6) (2019) 1387–1393. doi:10.1021/acsenergylett.9b00711. 2.5

[43] A. J. Yost, T. K. Ekanayaka, G. Gurung, G. Rimal, S. Horoz, J. Tang, T. Paudel, T. Chien, Influence of the cation on the surface electronic band structure and magnetic properties of mn: Zns and mn: Cds quantum dot thin films, The Journal of Physical Chemistry C 123 (40) (2019) 24890–24898. doi:10.1021/acs.jpcc.9b06551. 2.5

[44] F. Zakerian, H. Kafashan, Investigation the effect of annealing parameters on the physical properties of electrodeposited zns thin films, Superlattices and Microstructures 124 (2018) 92–106. doi:10.1016/j.spmi.2018.09.039. 2.5

[45] R. Shan, J. Yi, J. Zhong, S. Yang, Effect of sulphur pressure on properties of zns thin film prepared by chemical bath deposition technique, Journal of Materials Science: Materials in Electronics 30 (14) (2019) 13230–13237. doi:10.1007/s10854-019-01686-2. 2.5

[46] Y. I. Choi, S. Lee, S. K. Kim, Y.-I. Kim, D. W. Cho, M. M. Khan, Y. Sohn, Fabrication of zno, zns, ag-zns, and au-zns microspheres for photocatalytic activities, co oxidation and 2-hydroxyterephthalic acid synthesis, Journal of Alloys and Compounds 675 (2016) 46–56. doi:10.1016/j.jallcom.2016.03.070. 2.5

[47] F. Göde, E. Güneri, A. Kariper, C. Ulutaş, F. Kirmizigül, C. Gümüş, Influence of annealing temperature on the structural, optical and electrical properties of amorphous zinc sulfide thin films, in: Journal of Physics: Conference Series, Vol. 326, IOP Publishing, 2011, p. 012020. doi:10.1088/1742-6596/326/1/012020. 2.5

[48] X.-S. Fang, C.-H. Ye, L.-D. Zhang, Y.-H. Wang, Y.-C. Wu, Temperature-controlled catalytic growth of zns nanostructures by the evaporation of zns nanopowders, Advanced Functional Materials 15 (1) (2005) 63–68. doi:10.1002/adfm.200305008. 2.5

[49] S. P. Lonkar, V. V. Pillai, S. M. Alhassan, Facile and scalable production of heterostructured zns-zno/graphene nano-photocatalysts for environ-

mental remediation, Scientific reports 8 (1) (2018) 1–14. doi:10.1038/s41598-018-31539-7. 2.5

[50] S. Zhang, S.-H. Wei, A. Zunger, Intrinsic n-type versus p-type doping asymmetry and the defect physics of zno, Physical Review B 63 (7) (2001) 075205. doi:10.1103/PhysRevB.63.075205. 2.5

[51] K. Yang, B. Li, G. Zeng, Effects of temperature on properties of zns thin films deposited by pulsed laser deposition, Superlattices and Microstructures 130 (2019) 409–415. doi:10.1016/j.spmi.2019.05.009. 2.5

[52] G. Yuan, W. Zhang, W. Zhang, X. Fan, I. Bello, C. S. Lee, S. T. Lee, p-type conduction in nitrogen-doped zns nanoribbons, Applied Physics Letters 93 (21) (2008) 213102. doi:10.1063/1.3025846. 2.5

[53] S. Patel, A. Purohit, S. Chander, M. Dhaka, et al., Thermal annealing evolution to physical properties of zns thin films as buffer layer for solar cell applications, Physica E: Low-dimensional Systems and Nanostructures 101 (2018) 174–177. doi:10.1016/j.physe.2018.04.006. 2.5

[54] X. Deng, D. C. Sorescu, J. Lee, Single-layer zns supported on au (111): A combined xps, leed, stm and dft study, Surface Science 658 (2017) 9–14. doi:10.1016/j.susc.2016.12.003. 2.5

[55] J. Jenkin, R. Leckey, J. Liesegang, The development of x-ray photoelectron spectroscopy: 1900–1960, Journal of electron spectroscopy and related phenomena 12 (1) (1977) 1–35. doi:/10.1016/0368-2048(77)85065-2. 3.1

[56] S. Hofmann, Auger-and X-ray photoelectron spectroscopy in materials science: a user-oriented guide, Vol. 49, Springer Science & Business Media, 2012. 3.1, 3.1.2, 3.1.2

[57] G. Greczynski, L. Hultman, X-ray photoelectron spectroscopy: Towards reliable binding energy referencing, Progress in Materials Science 107 (2020) 100591. 3.1, 3.1.2, 3.3, 3.3, 3.11

[58] S. Hüfner, Photoelectron spectroscopy: principles and applications, Springer Science & Business Media, 2013. 3.1.1, 3.1.1, 3.1.1, 3.1, 3.1.2, 4

[59] E. Kötz, H. Neff, K. Müller, A ups, xps and work function study of emersed silver, platinum and gold electrodes, Journal of electroanalytical chemistry and interfacial electrochemistry 215 (1-2) (1986) 331–344. doi:10.1016/0022-0728(86)87026-7. 2

[60] F. A. Stevie, C. L. Donley, Introduction to x-ray photoelectron spectroscopy, Journal of Vacuum Science & Technology A: Vacuum, Surfaces, and Films 38 (6) (2020) 063204. doi:10.1116/6.0000412. 3.1.2, 3.1.2, 3.2, 3.10

[61] Peak fitting in casa xps, http://www.casaxps.com/help_manual/manual_updates/peak_fitting_in_xps.pdf. 3.1.2

[62] M. H. Engelhard, D. R. Baer, A. Herrera-Gomez, P. M. Sherwood, Introductory guide to backgrounds in xps spectra and their impact on determining peak intensities, Journal of Vacuum Science & Technology A: Vacuum, Surfaces, and Films 38 (6) (2020) 063203. 3.1.2

[63] X-ray emission sources, https://www.thermofisher.com/br/en/home/materials-science/learning-center/surface-analysis/x-ray-generation.html. 3.3

[64] J. Leiro, M. Heinonen, Surface plasmons in niga and coga alloys, Surface science 346 (1-3) (1996) 73–78. doi:10.1016/0039-6028(95)00916-7. 3.1.2

[65] M. A. Van Hove, S. Y. Tong, Surface crystallography by LEED: theory, computation and structural results, Vol. 2, Springer Science & Business Media, 2012. 3.2.1, 3.2.2, 3.6, 3.2.2

[66] H. Lüth, Solid surfaces, interfaces and thin films, Vol. 4, Springer, 2001. 3.2.2, 3.2.2, 3.2.2, 3.2.2, 3.5, 3.8, 3.3, 3.12, 3.3, 4.1

[67] Leedpat, version 4.2, utility by k.e. hermann (fhi) and m.a. van hove (hkbu), berlin / hong kong, 2014, http://www.fhi-berlin.mpg.de/KHsoftware/LEEDpat/index.html. 3.7, 4.2

[68] R. Sharpe, Surface science studies of pd and au on tio2(110) single crystals, http://orca.cf.ac.uk/id/eprint/76888, phd Thesis (2006). 3.3

[69] Vac AERO International, An introduction to vacuum pumps, https://vacaero.com/information-resources/vacuum-pump-technology-education-and-training/1039-an-introduction-to-vacuum-pumps.html, accessed: 2021-01-212. 3.3

[70] R. M. Nieminen, Supercell methods for defect calculations, Theory of Defects in Semiconductors (2007) 29–68doi:10.1007/11690320_3. 3.5

[71] A. Kokalj, Xcrysdena new program for displaying crystalline structures and electron densities, Journal of Molecular Graphics and Modelling 17 (3-4) (1999) 176–179. doi:10.1016/S1093-3263(99)00028-5. 3.13

[72] D. Sholl, J. A. Steckel, Density functional theory: a practical introduction, John Wiley & Sons, 2011. 3.5, 5

[73] P. Giannozzi, S. Baroni, N. Bonini, M. Calandra, R. Car, C. Cavazzoni, D. Ceresoli, G. L. Chiarotti, M. Cococcioni, I. Dabo, et al., Quantum espresso: a modular and open-source software project for quantum simulations of materials, Journal of physics: Condensed matter 21 (39) (2009) 395502. doi:doi.org/10.1088/0953-8984/21/39/395502. 3.5

[74] J. P. Perdew, K. Burke, M. Ernzerhof, Generalized gradient approximation made simple, Physical review letters 77 (18) (1996) 3865. doi:10.1103/PhysRevLett.77.3865. 3.5

[75] H. J. Monkhorst, J. D. Pack, Special points for brillouin-zone integrations, Physical review B 13 (12) (1976) 5188. doi:10.1103/PhysRevB.13.5188. 3.5

[76] M. Liu, S. Wang, C. Wang, G. Zhang, Y. Wang, X. Li, P. Shang, R. Zhang, Y. Ji, J. Chu, Understanding of electronic and optical properties of zns with high concentration of point defects induced by hot pressing process: The first-principles calculations, Computational Materials Science 174 (2020) 109492. doi:10.1016/j.commatsci.2019.109492. 4.1

[77] N. Dengo, A. Vittadini, M. M. Natile, S. Gross, In-depth study of zns nanoparticle surface properties with a combined experimental and theoretical approach, The Journal of Physical Chemistry C 124 (14) (2020) 7777–7789. doi:10.1021/acs.jpcc.9b11323. 4.1

[78] Thermo scientific reports, https://xpssimplified.com/elements/zinc.php, accessed: 2020-04-21. 4.1

[79] D. Barreca, A. Gasparotto, C. Maragno, E. Tondello, T. R. Spalding, Analysis of nanocrystalline zns thin films by xps, Surface Science Spectra 9 (1) (2002) 54–61. doi:10.1116/11.20030117. 4.1

[80] K. Laajalehto, I. Kartio, P. Nowak, Xps study of clean metal sulfide surfaces, Applied surface science 81 (1) (1994) 11–15. doi:10.1016/0169-4332(94)90080-9. 4.2

[81] G. Kellogg, Direct observations of the (1× 2) surface reconstruction on the pt (110) plane, Physical review letters 55 (20) (1985) 2168. doi:10.1103/PhysRevLett.55.2168. 4.2

[82] P. Hohenberg, W. Kohn, Inhomogeneous electron gas, Physical review 136 (3B) (1964) B864. doi:10.1103/PhysRev.136.B864. 5

[83] J. D. M. Vianna, Teoria Quântica de Moléculas e Sólidos: simulaçao computacional, Livraria da Física, 2004. 5, 5, 5, 5, 5, 5

[84] J. P. Perdew, W. Yang, K. Burke, Z. Yang, E. K. Gross, M. Scheffler, G. E. Scuseria, T. M. Henderson, I. Y. Zhang, A. Ruzsinszky, et al., Understanding band gaps of solids in generalized kohn–sham theory, Proceedings of the national academy of sciences 114 (11) (2017) 2801–2806. doi:10.1073/pnas.1621352114. 5

[85] H. Xiao, J. Tahir-Kheli, W. A. Goddard III, Accurate band gaps for semiconductors from density functional theory, The Journal of Physical Chemistry Letters 2 (3) (2011) 212–217. doi:10.1021/jz101565j. 5